

THE MAGNETIC BEHAVIOR OF
SEVERAL TRANSITION METAL SALTS-
SOME LOW-DIMENSIONAL EFFECTS

Dissertation for the Degree of Ph. D.
MICHIGAN STATE UNIVERSITY
CHARLES RALPH STIRRAT
1974



This is to certify that the

thesis entitled

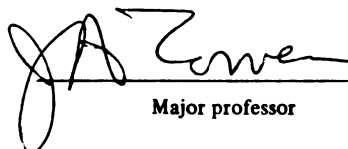
THE MAGNETIC BEHAVIOR OF
SEVERAL TRANSITION METAL SALTS -
SOME LOW-DIMENSIONAL EFFECTS

presented by

Charles Ralph Stirrat

has been accepted towards fulfillment
of the requirements for

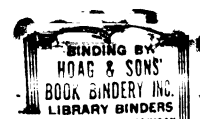
Ph.D. degree in Physics



Major professor

Date August 21, 1974

Q-7639



ABSTRACT

THE MAGNETIC BEHAVIOR OF SEVERAL TRANSITION METAL SALTS- SOME LOW-DIMENSIONAL EFFECTS

By

Charles Ralph Stirrat

Low-temperature magnetic measurements are reported on three transition metal salts, $((\text{CH}_3)_3\text{NH})\text{CuCl}_3 \cdot 2\text{H}_2\text{O}$, $((\text{CH}_3)_3\text{NH})\text{CoCl}_3 \cdot 2\text{H}_2\text{O}$, and $\text{NiI}_2 \cdot 6\text{H}_2\text{O}$. These measurements include electron spin resonance, nuclear magnetic resonance, and magnetic susceptibility in zero and applied field. The experimental results have been interpreted in terms of existing theories.

Trimethylamine copper chloride orders magnetically at $T_c = 0.157 \pm 0.003$ K. Above the transition the susceptibility is given by the high-temperature expansion for a two-dimensional square Heisenberg lattice with $J_F/k = 0.28 \pm 0.02$ K. Below T_c the crystal exhibits behavior characteristic of weak anti-ferromagnetic coupling between the ferromagnetic layers. The successive spins along a are canted slightly away from a due to the presence of two inequivalent anisotropic g-tensors.

The magnetic susceptibility of trimethylamine cobalt chloride in the ordered state ($T < T_N = 4.135$ K) exhibits metamag-

netic behavior. This field dependent behavior is explained qualitatively by a phenomenological model due to Spence and Botterman¹.

Nickel iodide hexahydrate orders magnetically at $T_c=0.120$ K. The paramagnetic behavior can be interpreted in terms of two nonequivalent Ni^{++} sites having $g=2.22$, zero field splitting parameters $D_1/k=1.60$ K, $D_2/k=2.30$ K and weak ferromagnetic exchange with $2zJ/k=+0.05$ K. The ^{127}I NMR can be explained assuming a quadrupole term with $\nu_Q=5.70\pm0.01$ MHz and $\eta=0$ and a transferred hyperfine tensor specified by $A_{||}=2.30\pm0.10$ MHz and $A_{\perp}=0.55\pm0.10$ MHz.

1. R. D. Spence and A. C. Botterman, Phys. Rev. B9, 2993 (1974).

THE MAGNETIC BEHAVIOR
OF SEVERAL TRANSITION METAL SALTS-
SOME LOW-DIMENSIONAL EFFECTS

By

Charles Ralph Stirrat

A DISSERTATION

Submitted to
Michigan State University
in partial fulfillment of the requirements
for the degree of

DOCTOR OF PHILOSOPHY

Department of Physics

1974

To my wife, Carolyn,
and
to my parents

ACKNOWLEDGEMENTS

The author wishes to thank Dr. J. A. Cowen for his patience, guidance and help in this work.

To Dr. R. D. Spence my gratitude for his interest and support.

A special thanks to Paul R. Newman for his help in the laboratory and willingness to listen.

TABLE OF CONTENTS

	Page
LIST OF TABLES	vi
LIST OF FIGURES	vii
INTRODUCTION	1
I. THEORETICAL BACKGROUND	3
II. EXPERIMENTAL TECHNIQUES AND APPARATUS	14
A. <u>Magnetic Susceptibility</u>	14
B. <u>Electron Spin Resonance (ESR)</u>	15
C. <u>Nuclear Magnetic Resonance (NMR)</u>	16
D. <u>Crystal Orientation</u>	25
III. $((\text{CH}_3)_3\text{NH})\text{CuCl}_3 \cdot 2\text{H}_2\text{O}$ - A TWO-DIMENSIONAL SQUARE HEISENBERG FERROMAGNET	26
A. <u>Crystal Structure and Preparation</u>	26
B. <u>Experimental Results</u>	29
1. ESR - Principal Axis Determination	29
2. Magnetic Susceptibility	30
C. <u>Interpretation of Results</u>	36
IV. $((\text{CH}_3)_3\text{NH})\text{CoCl}_3 \cdot 2\text{H}_2\text{O}$ - METAMAGNETIC BEHAVIOR	54
A. <u>Crystal Structure and Preparation</u>	54
B. <u>Experimental Results</u>	54
C. <u>Interpretation of Results</u>	58
V. $\text{NiI}_2 \cdot 6\text{H}_2\text{O}$ - CRYSTAL FIELD SPLITTING WITH WEAK EXCHANGE	74
A. <u>Crystal Structure and Preparation</u>	74

	Page
B. <u>Experimental Results</u>	75
1. ESR	75
2. Magnetic Susceptibility	75
3. NMR	86
C. <u>Interpretation of Results</u>	93
VI. CONCLUSIONS	106
REFERENCES	108

LIST OF TABLES

Table	Page
I. Principal g-tensor Values and Orientation. θ is measured from the c'-axis toward the ab plane and ϕ is measured from the a-axis toward the b-axis.	31
II. ^{127}I Quadrupole and Hyperfine Constants for paramagnetic $\text{NiI}_2 \cdot 6\text{H}_2\text{O}$.	104

LIST OF FIGURES

Figure	Page
1. Block diagram of pulsed NMR spectrometer.	19
2. Time sequence of mini-pulser and boxcar integrator operation.	21
3. Sample recording using the pulsed NMR spectrometer.	23
4. Angle dependence of the ESR of $((\text{CH}_3)_3\text{NH})\text{CuCl}_3 \cdot 2\text{H}_2\text{O}$ in the ac' plane plotted as g^2 vs. θ . The curves are the least squares result used in the principal axis determination.	28
5. Inverse magnetic susceptibilities of $((\text{CH}_3)_3\text{NH})\text{CuCl}_3 \cdot 2\text{H}_2\text{O}$ measured parallel to the a , b , and c axes.	33
6. Magnetic susceptibilities of $((\text{CH}_3)_3\text{NH})\text{CuCl}_3 \cdot 2\text{H}_2\text{O}$ measured parallel to the a , b , and c axes near the transition temperature.	35
7. The magnetic susceptibility of $((\text{CH}_3)_3\text{NH})\text{CuCl}_3 \cdot 2\text{H}_2\text{O}$ measured parallel to the c -axis plotted as $C/\chi T$ vs. J/kT . Solid curve (1) is the Curie-Weiss result with $\theta = 2J/k$, (2) is the square Heisenberg ferromagnet, and (3) is the Heisenberg ferromagnetic chain (abscissa scaled down by a factor of 2). ($J/kT = 0.5$ corresponds to $T = 0.56$ K)	39
8. The various coordinate systems used to show canting due to g -tensor inequivalence. xyz is the crystal system; $x'y'z'$ is the system in which the g -tensor is diagonal; $x''y''z''$ is the system in which \vec{s} lies along y'' in equilibrium.	45
9. The relationship between the effective spin \vec{s}_1 and magnetic moment \vec{m}_1 .	48
10. Proposed ordered state spin arrangement for $((\text{CH}_3)_3\text{NH})\text{CuCl}_3 \cdot 2\text{H}_2\text{O}$. The spins lie in the ac plane.	52

Figure	Page
11. The field dependence of the magnetic susceptibility of $((\text{CH}_3)_3\text{NH})\text{CoCl}_3 \cdot 2\text{H}_2\text{O}$. (a) The open squares are experimental results for HMc. The solid line is the theoretical prediction for $\theta=0^\circ$; the dashed line is the theoretical prediction for $\theta=3^\circ$. (b) Data and theory for HNa ($\theta=90^\circ$).	57
12. χ vs. θ with $H=300$ Oe for $((\text{CH}_3)_3\text{NH})\text{CoCl}_3 \cdot 2\text{H}_2\text{O}$.	60
13. χ vs. θ with $H=438$ Oe for $((\text{CH}_3)_3\text{NH})\text{CoCl}_3 \cdot 2\text{H}_2\text{O}$.	60
14. χ vs. θ with $H=976$ Oe for $((\text{CH}_3)_3\text{NH})\text{CoCl}_3 \cdot 2\text{H}_2\text{O}$.	62
15. χ vs. θ with $H=1075$ Oe for $((\text{CH}_3)_3\text{NH})\text{CoCl}_3 \cdot 2\text{H}_2\text{O}$.	62
16. The spin configurations C_1 , C_2 , and C_3 assumed by the Spence ² model.	64
17. Regions of magnetization in the $H\theta$ plane.	68
18. ESR rotation patterns in the ac plane ($\theta=0^\circ$ is the c-axis) for $\text{NiI}_2 \cdot 6\text{H}_2\text{O}$ at $\nu=10.01$ GHz and $T=1.1$ K. The solid ² lines are the theoretical predictions.	77
19. ESR rotation patterns in the ac plane ($\theta=0^\circ$ is the c-axis) for $\text{NiI}_2 \cdot 6\text{H}_2\text{O}$ at $\nu=24.45$ GHz and $T=1.1$ K. The solid ² lines are the theoretical predictions.	79
20. Resonant frequency vs. field applied parallel to the c-axis for $\text{NiI}_2 \cdot 6\text{H}_2\text{O}$. The solid and dashed lines are theoretical predictions.	81
21. Inverse magnetic susceptibility of $\text{NiI}_2 \cdot 6\text{H}_2\text{O}$ measured parallel to the a and c axes. ² The solid lines are the theoretical results using equations (5.3)-(5.8).	83
22. Magnetic susceptibility of $\text{NiI}_2 \cdot 6\text{H}_2\text{O}$ measured parallel to the a and c axes below ² 1.4 K.	85
23. ^{127}I NMR frequency vs. magnetic field applied perpendicular to c for $\text{NiI}_2 \cdot 6\text{H}_2\text{O}$.	88
24. ^{127}I NMR frequency vs. magnetic field applied parallel to c for $\text{NiI}_2 \cdot 6\text{H}_2\text{O}$.	90
25. Temperature dependence of the $m_I=+1/2 \leftrightarrow m_I=-1/2$ resonance line of ^{127}I in $\text{NiI}_2 \cdot 6\text{H}_2\text{O}$ for $\nu=13.1$ MHz.	92

26. Energy level diagram of Ni^{++} ($S=1$) as a function of magnetic field, H , parallel to z with $D>0$ (doublet lowest). 96

INTRODUCTION

The magnetic properties of transition metal salts have been studied by experimentalists and theorists for a long time. Historically the interplay between experiment and theory has been varied and complex. Sometimes an experiment will produce new and unexpected results which require the development of a new theory to explain them. At other times theorists have predicted behavior long before it was experimentally observed. In this thesis experiments designed to substantiate existing theories are reported. Failure of the theories to predict experimental results indicates the inappropriateness of a particular model or the need for expanded theoretical work.

An exact theoretical description of the magnetic properties of any real crystal is an impossibility because of the number of particles involved. Therefore most theories project out of the exact description those terms which adequately describe the situation of interest and yet are amenable to calculation. One assumption, currently the subject of much theoretical work, is that the exchange interaction in one or more directions is negligible. This leads to a "low-dimensional" model in which a linear(one-dimensional) or planar(two-dimensional) lattice, rather than a three-dimensional lattice, is considered.

Experiments on three salts; trimethylamine copper chloride, trimethylamine cobalt chloride, and nickel iodide; are

reported in this thesis. The interpretation of the results involves models with varied assumptions as to what interactions are important. The trimethylamine salts exhibit low-dimensionality while nickel iodide does not. A short summary of the theoretical models and some of the assumptions they imply is given in Section I.

Section II describes the experimental apparatus and the techniques used for the measurements reported in this thesis. The experiments include magnetic susceptibility, electron spin resonance(ESR), and nuclear magnetic resonance(NMR).

The experimental results and interpretation of measurements on $((\text{CH}_3)_3\text{NH})\text{CuCl}_3 \cdot 2\text{H}_2\text{O}$ are given in Section III. A two-dimensional-square Heisenberg lattice is appropriate for trimethylamine copper chloride.

In Section IV results of field dependent magnetic susceptibility measurements on $((\text{CH}_3)_3\text{NH})\text{CoCl}_3 \cdot 2\text{H}_2\text{O}$ are reported. Prior work has shown this salt to be described by a two-dimensional rectangular Ising lattice¹. The salt exhibits unusual metamagnetic behavior in applied field² and the measurements included here reflect this behavior.

In Section V ESR and susceptibility experiments are described which show that the exchange interaction in $\text{NiI}_2 \cdot 6\text{H}_2\text{O}$ is less important than the electrostatic crystal field interaction. NMR measurements are also discussed.

In addition, for each of the three salts, three dimensional magnetic order was observed at sufficiently low temperatures.

I. THEORETICAL BACKGROUND

The magnetic properties of transition metal salts are due to the orbital and intrinsic spin angular momenta of unpaired electrons. Therefore any theoretical model, other than a purely phenomenological one, must describe this system of electrons. A general Hamiltonian^{3,4} can be written:

$$\mathcal{H} = \mathcal{H}_{\text{INTRA}} + \mathcal{H}_{\text{CF}} + \mathcal{H}_{\text{SO}} + \mathcal{H}_{\text{Z}} + \mathcal{H}_{\text{DD}} + \mathcal{H}_{\text{HF}} \quad (1.1)$$

The first term, $\mathcal{H}_{\text{INTRA}}$, includes the intraatomic Coulomb interactions between the electronic and nuclear charges. Most theories treat this term using a product of single electron wave functions as a first approximation for the intraatomic wave functions. These one-electron functions are the solutions for the electron moving in the Coulomb potential of the nucleus. The ground state of the ion is determined by $\mathcal{H}_{\text{INTRA}}$ but its configuration is summarized by Hund's rule. The rule states that the minimum energy configuration will have the maximum possible spin S , and that the orbital angular momentum, L , will have the largest value that can be associated with that maximum S .

The Coulomb interactions between each electron and the charges external to the ion are included in the second term, \mathcal{H}_{CF} . This crystal field term treats the potential $V(\vec{r})$ seen by the electron as being due to point charges at the sites of other ions. A more complete calculation involves treating the spatial distribution of charge on the neighboring sites. Such a ligand field theory can be employed when the

neighboring ion orbitals overlap the electron orbitals of interest. It is easier and usually sufficient to use the crystal field approach. The symmetry of the lattice is reflected in $V(\vec{r})$ so that group theory provides a means of determining the degeneracy of the levels resulting after \mathcal{H}_{CF} splits the degenerate ground state of the isolated ion.

The combination of \mathcal{H}_{INTRA} and \mathcal{H}_{CF} allows the characterization of the ion's ground state by a total orbital angular momentum, \vec{L} , and total spin angular momentum, \vec{S} .

The spin-orbit term, \mathcal{H}_{SO} , represents the interaction between the orbital angular momentum and the intrinsic spin angular momentum. The contribution for each ion can be written

$$\mathcal{H}_{SO}^i = \lambda \vec{L}_i \cdot \vec{S}_i \quad (1.2)$$

where \vec{L} and \vec{S} are defined above and λ is the spin-orbit parameter. Although \mathcal{H}_{SO} couples \vec{L} and \vec{S} , for the iron group transition metals, \mathcal{H}_{CF} normally dominates \mathcal{H}_{SO} and the characterization of the ground state in terms of \vec{L} and \vec{S} is still appropriate.

\mathcal{H}_Z^i , the Zeeman term, involves the interaction between the magnetic moment of the ion, $\vec{\mu}_i$, and a uniform external magnetic field, \vec{H} . Thus

$$\mathcal{H}_Z^i = -\vec{\mu}_i \cdot \vec{H} = \mu_B (\vec{L}_i + 2\vec{S}_i) \cdot \vec{H} \quad (1.3)$$

where μ_B is the Bohr magneton.

The magnetic dipole-dipole contribution, \mathcal{H}_{DD}^{ij} , for the magnetic moments at sites i and j separated by \vec{r}_{ij} is given

by

$$\mathcal{H}_{DD}^{ij} = \frac{\vec{\mu}_i \cdot \vec{\mu}_j - 3(\vec{\mu}_i \cdot \hat{r}_{ij})(\vec{\mu}_j \cdot \hat{r}_{ij})}{r_{ij}^3} \quad (1.4)$$

The hyperfine term, \mathcal{H}_{HF} , involves the interaction between the nuclear magnetic moment and the electronic magnetic moment. For most problems it is only a small perturbation on the electronic energy levels, but it can be very important in considering the nuclear energy levels (Section V). It consists of an orbital term, a contact term and a dipolar term. The last two are included in the magnetic hyperfine coupling tensor, \vec{A} . Thus

$$\mathcal{H}_{HF} = -2\mu_B \gamma_N \hbar \frac{\vec{I} \cdot \vec{L}}{r^3} + \vec{I} \cdot \vec{A} \cdot \vec{S} \quad (1.5)$$

where γ_N is the nuclear gyromagnetic ratio and \vec{I} is the nuclear spin. \mathcal{H}_{HF} is considered negligible in treating the electronic magnetic properties.

The use of one-electron wave functions for \mathcal{H}_{INTRA} fails to predict behavior resulting from the fact that the solution should be antisymmetric. Adding a term of the form

$$\mathcal{H}_{EX}^{ij} = -2J_{ij} \vec{S}_i \cdot \vec{S}_j \quad (1.6)$$

will include some of the effects lost by failing to use antisymmetric solutions. This is known as the Heisenberg exchange Hamiltonian. J_{ij} , the exchange energy between sites i and j , is greater than zero for ferromagnetic exchange and less than zero for antiferromagnetic exchange. It is also

possible to have "superexchange" where the magnetic ion wavefunctions overlap the wavefunctions of an intervening anion, thus increasing the effective exchange between the two sites.

Because of its many-body nature, the solution of this general Hamiltonian (1.1) is impossible; however, it is often possible to project out of \mathcal{H} the terms that adequately describe the properties of interest. This is done by using a spin Hamiltonian³ in which the orbital contribution does not appear explicitly.

A spin treatment of the 3d transition metal salts is especially appropriate because the expectation value of each component of L for these ions in a crystal field is zero. This "quenching of the orbital angular momentum" by the crystal field greatly reduces the contribution of the orbital angular momentum to the magnetic moment. Although $\langle L_x \rangle = \langle L_y \rangle = \langle L_z \rangle = 0$, the magnitude of L may be nonzero.

If the crystal has a symmetry such that the orbital degeneracy of the ground state is completely lifted, then to first order in λ , $\langle \vec{L} \rangle = 0$. The higher order orbital contributions can be included as an anisotropic g -tensor:

$$\vec{\mu}_i = \mu_B \vec{g} \cdot \vec{S}_i, \quad (1.7)$$

where g does not differ greatly from the free electron value, $g=2.0023$. The spin Hamiltonian corresponding to \mathcal{H}_Z , \mathcal{H}_{SO} , and the zero-field splitting of the spin states contained in \mathcal{H}_{CF} can be written, for a single ion spin, \vec{S}_i , as

$$\mathcal{H}_S^i = \mu_B \vec{H} \cdot \vec{g} \cdot \vec{S}_i + D S_{zi}^2 + E(S_{xi}^2 - S_{yi}^2). \quad (1.8)$$

It is often possible to use the spin Hamiltonian formalism even if the orbital degeneracy of the ground state is not lifted by \mathcal{H}_{CF} and $L \neq 0$. \vec{S} must be replaced by an effective spin, \vec{s} , which is chosen so that the number of states into which the ground state splits in an applied field is $(2s+1)$. In such cases the spin-orbit interaction produces first order shifts of the energy, and thus the g-factors will differ significantly from the free electron value. For example in a cubic crystal field Co^{++} has a ground state with $L=1$, $S=3/2$. The spin-orbit interaction splits this 12-fold degenerate level so that a doublet lies lowest. Thus at low temperatures Co^{++} can be treated as having effective spin $s=1/2$ with a very anisotropic g-tensor. Using an effective spin Hamiltonian implies no zero-field splitting so

$$\vec{\mu}_i = \mu_B \vec{g} \cdot \vec{s}_i \quad (1.9)$$

and

$$\mathcal{H}_s^i = \mu_B \vec{H} \cdot \vec{g} \cdot \vec{s}_i \quad (1.10)$$

Thus the spin Hamiltonian formalism can be used either with \vec{S} or \vec{s} depending on the orbital degeneracy of the ground state. In the rest of this section the spin is denoted by \vec{S} but if $L \neq 0$ then \vec{s} should be used along with equations (1.9) and (1.10) instead of (1.7) and (1.8).

In addition to the single spin terms considered above, one may include two-spin interactions, exchange and dipole-dipole in the spin Hamiltonian formalism. In the term \mathcal{H}_{DD}^{ij} one uses $\vec{\mu}_i$ determined by equation (1.7). The exchange

contribution is

$$\mathcal{H}_{EX} = 1/2 \sum_{ij} \mathcal{H}_{EX}^{ij} \quad (1.11)$$

where the sum is over all pairs of spins, $i \neq j$, but it is usually sufficient to consider nearest neighbor spins only.

Although a simple form for the exchange term is given in equation (1.6), the most general form is written in terms of the exchange dyadic, \vec{J}_{ij} , as

$$\mathcal{H}_{EX}^{ij} = -2 \vec{S}_i \cdot \vec{J}_{ij} \cdot \vec{S}_j \quad (1.12)$$

If \vec{J}_{ij} has only symmetric elements, then (1.12) reduces to the Heisenberg Hamiltonian,

$$\mathcal{H}_{HEIS}^{ij} = -2(J_{xx}^{ij} S_{ix} S_{jx} + J_{yy}^{ij} S_{iy} S_{jy} + J_{zz}^{ij} S_{iz} S_{jz}) \quad (1.13)$$

The case $J_{xx}^{ij} = J_{yy}^{ij} = 0$ is known as the Ising Hamiltonian.

If the antisymmetric elements of \vec{J}_{ij} are nonzero, the antisymmetric part of equation (1.12) can be written in the form

$$\mathcal{H}_{AS}^{ij} = \vec{D}_{ij} \cdot \vec{S}_i \times \vec{S}_j \quad (1.14)$$

which may lead to canting of the spins. In many problems the antisymmetric terms may be neglected.

Thus the total spin Hamiltonian can be written as

$$\mathcal{H}_S = \sum_i \mathcal{H}_S^i + 1/2 \sum_{ij} \mathcal{H}_S^{ij}, \quad (1.15)$$

where $\mathcal{H}_S^{ij} = \mathcal{H}_{EX}^{ij} + \mathcal{H}_{DD}^{ij}$.

The eigenvalues of \mathcal{H}_S can, in principle, be found and used to calculate the statistical average for such magnetic quantities as magnetization, magnetic specific heat, and

magnetic susceptibility. This is done using the total density operator ρ . The thermal equilibrium value of an operator Q is given by⁵

$$\langle Q \rangle = \text{Tr}(\rho Q) = \frac{\text{Tr}(Q e^{-\mathcal{H}_S/kT})}{\text{Tr}(e^{-\mathcal{H}_S/kT})}. \quad (1.16)$$

In practice the eigenvalues for \mathcal{H}_S can be found only for special cases since the problem is still a many-body problem. A number of methods will be used here to handle this problem including single ion treatments, molecular fields, high-temperature expansions, and low-dimensionality.

If $\mathcal{H}_S^{ij} \ll \mathcal{H}_S^i$ it is often possible to consider the case of noninteracting spins. Then the eigenvalues of \mathcal{H}_S^i can be found since $\mathcal{H}_S = \sum_i \mathcal{H}_S^i$ and the density operator becomes $\rho = \sum_i \rho_i$ so

$$\langle Q \rangle = \sum_i \frac{\text{Tr}(Q e^{-\mathcal{H}_S^i/kT})}{\text{Tr}(e^{-\mathcal{H}_S^i/kT})}. \quad (1.17)$$

A system of noninteracting magnetic moments describable by \mathcal{H}_S with $\mathcal{H}_S^{ij}=0$ will have a magnetic susceptibility, $\chi_{\mu\nu} \equiv \frac{dM_\mu}{dH_\nu}$ that is temperature dependent. Such behavior is described as paramagnetic. At high temperature the zero-field susceptibility of a system of spins, each described by equation (1.8), is given by the Curie-Weiss law,

$$\chi_{\mu\nu} = \frac{C_{\mu\nu}}{T - \theta_{\mu\nu}} \quad (1.18)$$

where $C_{\mu\nu} = N_0 g_{\mu\nu}^2 \mu_B^2 S(S+1)/3k$ and θ contains terms proportional to D and E .

If \mathcal{H}_{EX}^{ij} is not negligible one may assume that the exchange

produces an effective field at site i proportional to the average magnetization of the rest of the sample. Thus in the molecular field approximation⁵ for isotropic exchange

$$\mathcal{H}_{EX}^{ij} \sim -2J_{ij} \langle \vec{S}_j \rangle \cdot \vec{S}_i, \quad (1.19)$$

where $\langle \vec{S}_j \rangle$ is determined from $\vec{M} = Ng\mu_B \langle \vec{S}_j \rangle$. In this approximation the total Hamiltonian can be written as the sum of \mathcal{H}^i 's so that the methods employed in the single ion case can still be used. The molecular field treatment often gives good qualitative results, but fails quantitatively due to the correlation effects that are neglected.

If the only exchange contribution of significance is an isotropic exchange, J , with z nearest neighbors then the molecular field approximation predicts that the high temperature susceptibility is still given by the Curie-Weiss law but θ now includes a term $\theta_{ex} = 2zJS(S+1)/3k$.

Another method used in calculating thermodynamic quantities from equations (1.15) and (1.16) is to expand ρ , the density operator, as a series in ascending negative powers of the temperature⁴. For example, a high temperature expansion for the partition function written in terms of $\beta \equiv 1/kT$ is given by

$$\begin{aligned} Z &\equiv \text{Tr}(e^{-\beta \mathcal{H}_S}) \\ &= 1 - (\text{Tr} \mathcal{H}_S) \beta + (\text{Tr} \mathcal{H}_S^2) \frac{\beta^2}{2!} - (\text{Tr} \mathcal{H}_S^3) \frac{\beta^3}{3!} + \cdots \end{aligned} \quad (1.20)$$

Such calculations are exact to the extent that, unlike the molecular field approximation, no approximation is made for

\mathcal{N}_S . Such an expansion is valid only for T such that the series converges. This condition is given qualitatively by $E \ll kT$. In practice the exact solution for \mathcal{N}_S is not obtained because the labor involved in calculating the higher order terms becomes prohibitive.

Consider a high temperature expansion for the zero field susceptibility with D and $E=0$ and nearest neighbor isotropic exchange⁶. Then for $H \parallel z$

$$\mathcal{N}_S = -2J \sum_{i,j} \vec{S}_i \cdot \vec{S}_j + g\mu_B H \sum_i S_{zi}, \quad (1.21)$$

where the sum is over nearest neighbor spins. This can be used in equation (1.20) along with

$$\chi = \frac{\partial^2}{\partial H^2} (kT \ln Z) \quad (1.22)$$

to obtain a high temperature expansion for χ in powers of J/kT . Estimates of the ordering temperature, T_c , can be made by determining the lower limit on T for which the series converges if the sequence of coefficients behaves regularly.

The sums in equation (1.15) are sums over the lattice sites occupied by the spins. The calculation of these sums is much easier for a linear chain(one-dimensional), a planar lattice(two-dimensional), or a cubic lattice than for the more complicated three-dimensional lattices characteristic of many transition metal salts. The results of such "low-dimensional" or simple lattice calculations can be applied if the exchange between a given spin and its neighbors can be characterized by three exchange parameters, J_1 , J_2 , and J_3 , corresponding

to the exchange parallel to three orthogonal directions in the crystal. For convenience the directions can be chosen so that $J_1 \geq J_2 \geq J_3$. A three dimensional system where $J_1 \gg J_2 \geq J_3$, can be approximated by a linear chain with nearest neighbor exchange, J_1 .

A "low-dimensional" model may apply for structures in which the magnetic ions are separated by nonmagnetic organic complexes in one or two directions but not in the others. Conversely the presence of certain anions between the magnetic ions in one direction can enhance the exchange in that direction through the mechanism of "superexchange."

For spins situated on a primitive orthogonal lattice, there will be a one-to-one correspondence between the J_{ij} 's and J_1 , J_2 , and J_3 . If the spins are not on such a lattice, the connection will not be as simple but J_1 , J_2 , and J_3 can often still be used. Consider a three dimensional lattice composed of layers in which the spins form a square lattice but the spins in successive layers are not directly above their neighbors. Then $J_1 = J_2$ for spin i would equal J_{ij} where j refers to the four nearest neighbor spins in the plane. J_3 might correspond to an effective exchange between spin i and several near spins in the plane above or below spin i .

In conclusion, although the complete description of the magnetic properties of a transition metal salt must involve a description of the orbital and spin angular momentum of the unpaired electrons, it is often possible to obtain important information using only a spin Hamiltonian. Even the solution

of this problem is often too difficult if two-spin processes, like exchange, are important. In these cases it is necessary to use one or more of the methods outlined above including molecular fields, high-temperature expansions, or low-dimensionality to make the problem tractable.

II. EXPERIMENTAL TECHNIQUES AND APPARATUS

A. Magnetic Susceptibility

Magnetic susceptibility was measured by a mutual inductance technique^{7,8} at 17 Hertz using a Cryotronics Model 17B⁹ mutual inductance bridge. Mutual inductance coils were wound to fit three different cryostats. In each case the coils were wound with a single primary and multiple secondary windings with sections wound oppositely so that the total mutual inductance of the empty system was approximately zero. The measuring field was less than 5 Oe.

Absolute measurements of $\chi(T, \theta)$ were made in an immersion ⁴He cryostat in which the sample could be removed from the coil at each temperature. The sample was mounted on an epoxy rotor which had a relative accuracy of 1°, and an absolute accuracy of ±3°. This apparatus was calibrated with a single crystal of Ferric Ammonium Alum to give an accuracy of approximately 10^{-6} emu/gm for a 0.1 gm sample. Sample masses were between 0.1 and 0.3 gm.

Temperatures from 0.025 K to 1.5 K were achieved with a ³He-⁴He dilution refrigerator. The sample is fixed so that only relative values were obtained. More-or-less absolute values were achieved by normalizing the results obtained with this apparatus near 1.5 K to those obtained with the ⁴He apparatus in the same temperature region. The temperature was determined with a carbon resistance thermometer which has been

calibrated using the temperature dependence of the magnetic susceptibility of a pellet of Cerium Magnesium Nitrate powder. This calibration is good to ± 0.005 K. Thus, although the numerical value of χ is not very accurate, the temperature at which, for example, magnetic ordering takes place is well determined.

The field dependence of the susceptibility was measured in a second ^4He immersion cryostat which consisted of a single horizontal axis rotor surrounded by a set of mutual inductance coils whose axis was, as in all three cryostats, vertical. These were in turn surrounded by and coaxial to a superconducting solenoid. Although it was possible to remove the sample and rotor from the measuring coil, the balance and sensitivity of the mutual inductance coils was a strong function of the field produced by the solenoid so that only relative values of χ could be determined. The solenoid produced approximately 17 kOe with an excitation current of 10 amperes. From rather crude measurements, the homogeneity of the field was estimated to be 0.3% over a 1 cm sphere, which is slightly larger than the size of samples used. This produced some broadening of the field dependent susceptibilities determined in Section V¹⁰.

B. Electron Spin Resonance (ESR)

A variety of ESR spectrometers was employed to obtain the data reported on in Section III and V. Simple reflection type spectrometers operating from 8 to 11, 13 to 15, and 22 to 25

GHz were used in conjunction with a large electromagnet capable of producing 20 kOe. For those cases where frequency dependence was of interest, the samples were mounted on the narrow wall of a shorted piece of rectangular waveguide. For those cases where more accurate values of g or stronger signals were desired, either rectangular TE_{102} or cylindrical TE_{011} cavities were used. Measurements were made at 300, 77, and from 1-4 K in a ^4He immersion cryostat.

C. Nuclear Magnetic Resonance (NMR)

Here too a variety of techniques were used. Marginal oscillator and free-induction spectrometers were used in ^4He , ^3He , and ^3He - ^4He dilution refrigerators with and without applied magnetic fields. Frequencies between 2 and 20 MHz and fields from zero to 20 kOe were used with different cryostats at different times. For example, pure quadrupole resonances of ^{127}I in $\text{NiI}_2 \cdot 6\text{H}_2\text{O}$ were observed in an AC modulation field using the marginal oscillator and the ^4He immersion cryostat at temperatures between 1 and 4 K. No pure quadrupole resonances were observed below 1 K in either the ^3He cryostat or the ^3He - ^4He cryostat for different reasons. In the ^3He cryostat the sample is immersed in the liquid ^3He which is contained in a small dewar that is in turn immersed in the ^4He . The NMR coil is wound on the outside of the small dewar giving a filling factor less than 0.2. The dilution refrigerator also has a very small filling factor - the sample is immersed in the ^3He - ^4He mixture and the coil is

wound on an epoxy form which is far from the sample chamber. In addition one may not use an AC modulation field because of eddy current heating; thus the marginal oscillator, which is the more sensitive of the two NMR spectrometers, may not be used.

Zeeman splitting of the ^{127}I resonances was observed in all cryostats using both spectrometers, but quantitative data was only obtained above the transition ($T_c = .120\text{ K}$) due to presumed rf heating.

The free induction spectrometer is a "mini pulser" developed by S. I. Parks¹¹. It consists of a low level rf oscillator, an rf pulse amplifier, a rf receiver and detector operating with a single coil. The apparatus is unique and operates as follows. A small rf signal at frequency ω_0 is continually applied to the rf receiver. A pulse sequence triggers the rf pulse amplifier which applies an rf pulse (of frequency ω_0) to the coil. If the external magnetic field is adjusted so that the NMR frequency, ω , is approximately equal to ω_0 the magnetization is tipped through an angle θ and precesses at ω . The signal induced in the coil is fed to the rf receiver-detector combination producing a beat frequency at $\omega - \omega_0$ which decays in time as the net transverse magnetization decays. This repetitive pattern is normally presented on an oscilloscope. The amplitude of the free induction beat pattern is a complicated function of $\omega - \omega_0$ but when the field is adjusted to be at the center of the resonance line, $\omega - \omega_0 = 0$, the beat frequency is zero.

Figure 1. Block diagram of pulsed NMR spectrometer.

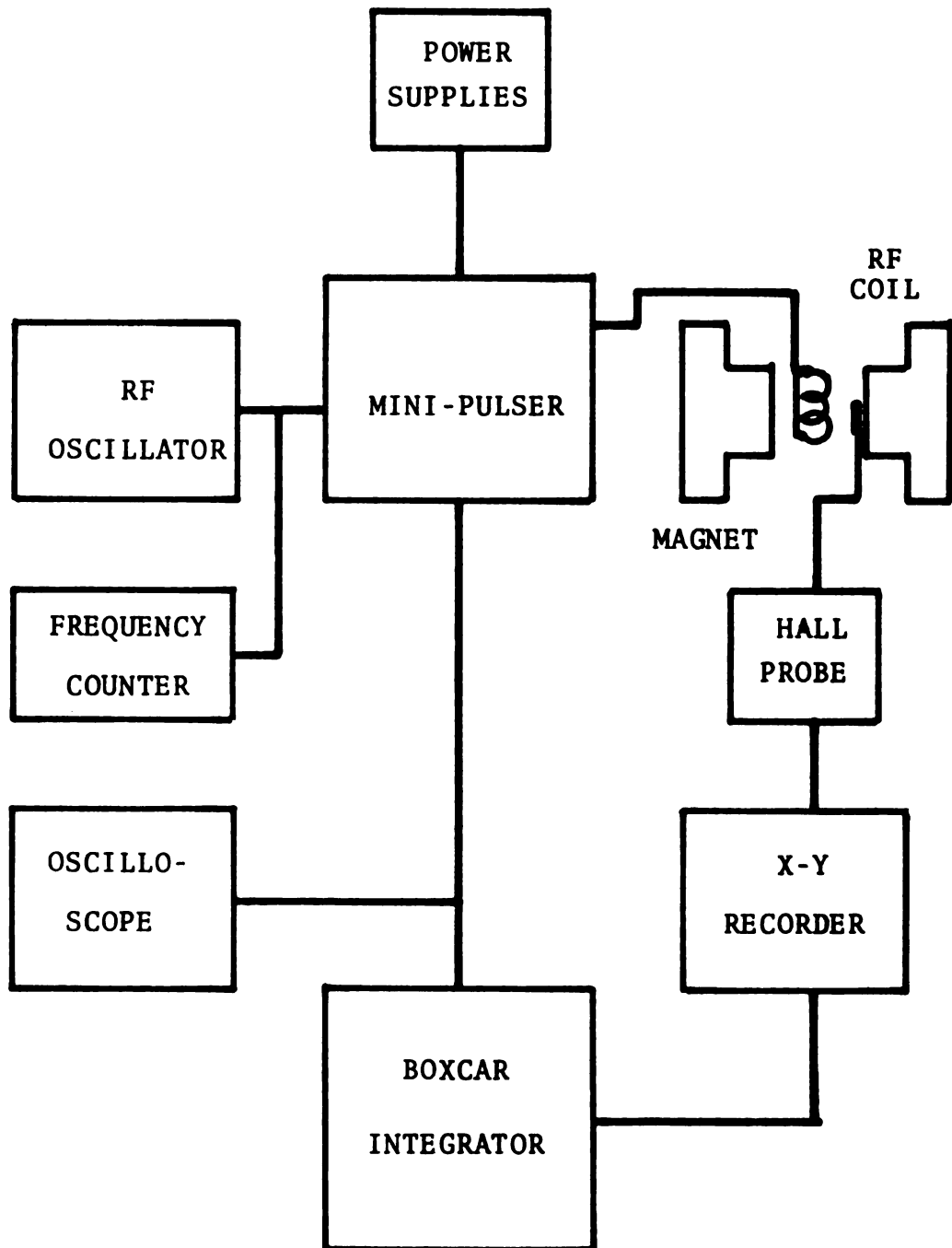


Figure 1

Figure 2. Time sequence of mini-pulser and boxcar integrator operation.

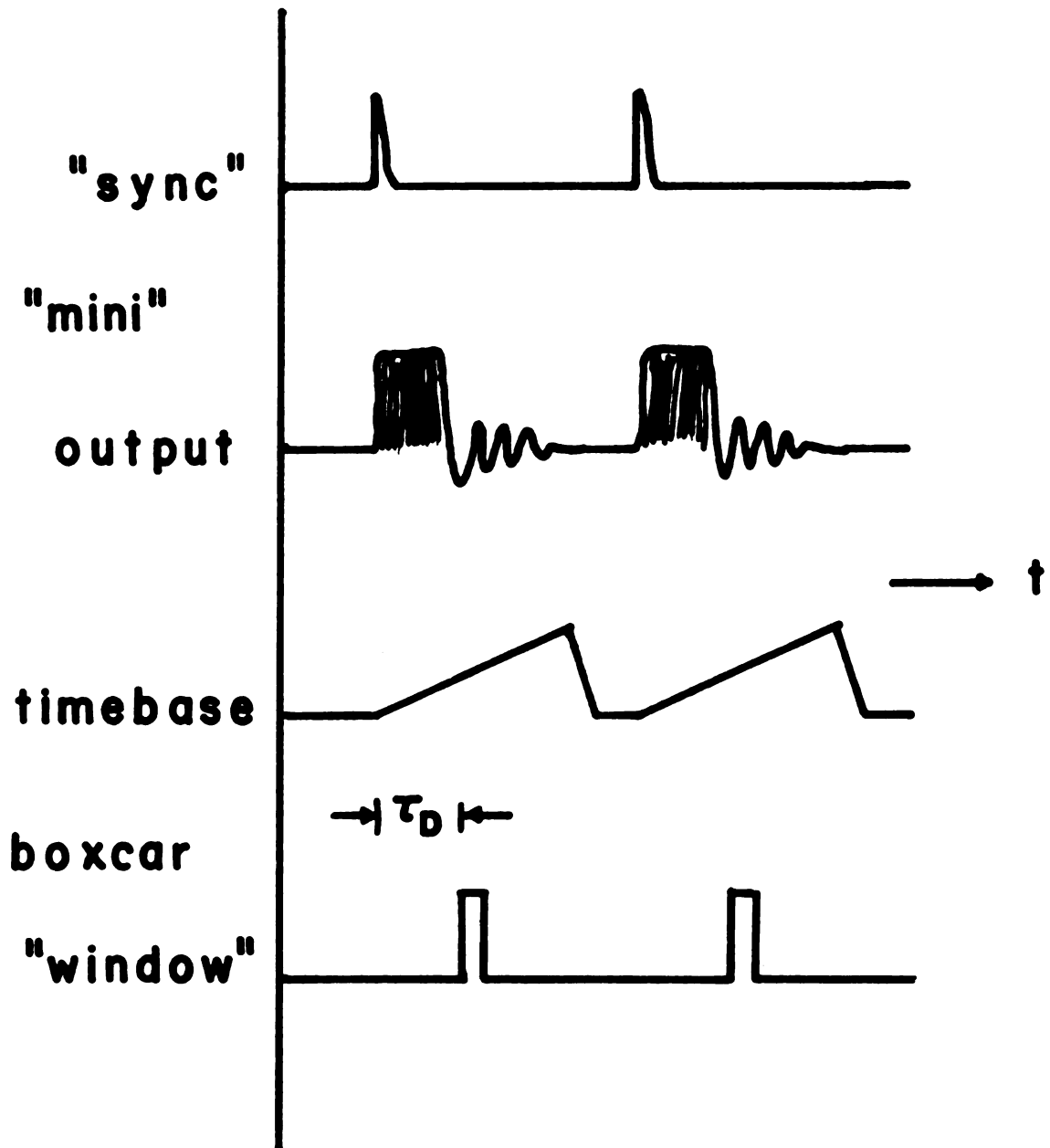


Figure 2

Figure 3. Sample recording using the pulsed NMR spectrometer.

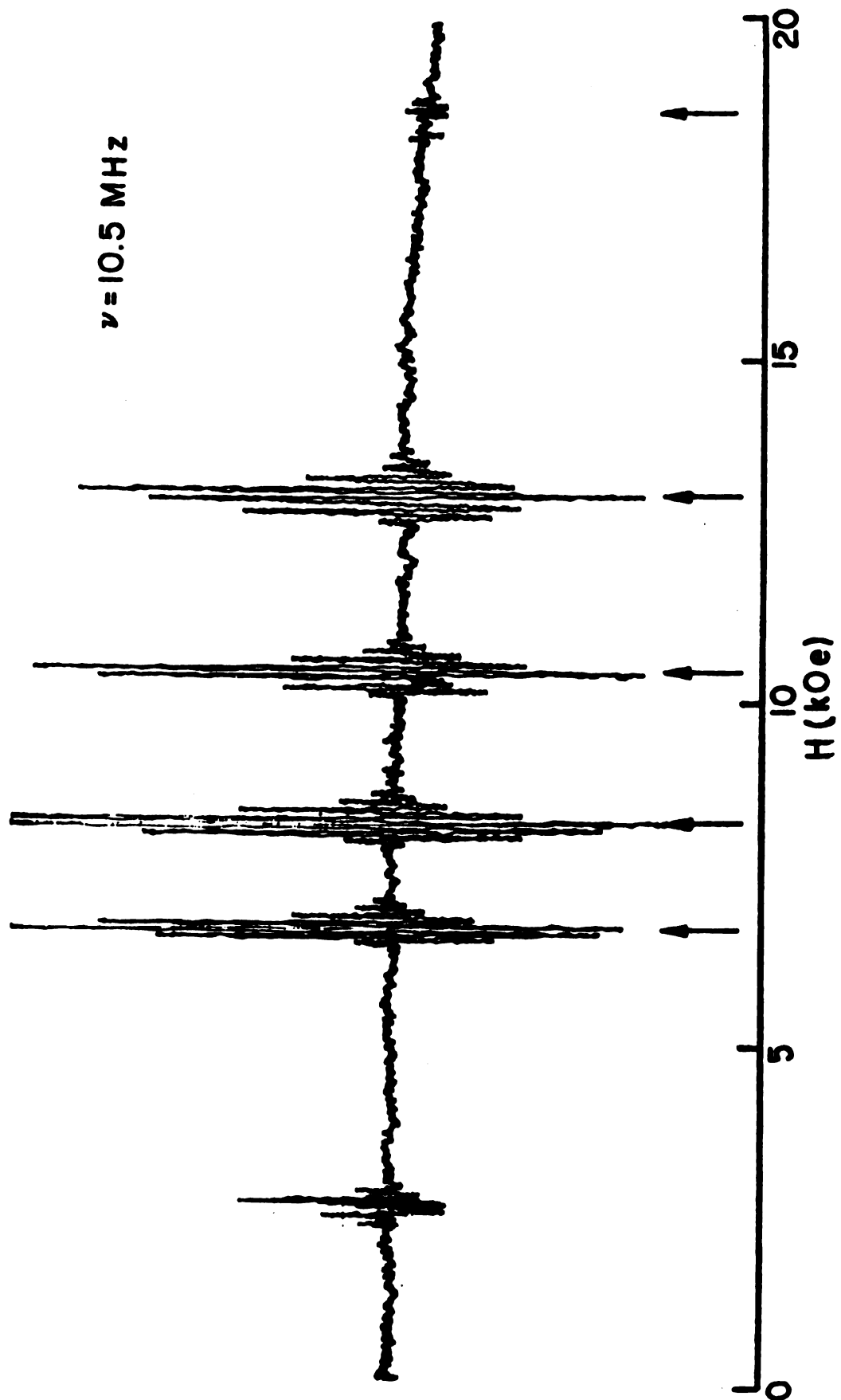


Figure 3

The mini pulser as described is relatively sensitive and needs no modulation field. Its disadvantages, as compared to the marginal oscillator, are complexity of tuning (there are several rf stages to tune) and the relative difficulty of determining from the scope the exact field at which zero beat occurs. By comparison the marginal oscillator is normally used with first or second derivative detection and for well resolved lines the resonant field is quite accurately determined.

Mr. Paul Newman of our laboratory suggested a very nice scheme for overcoming this last limitation which uses a Boxcar integrator. A block diagram of the system is shown in Figure 1. Each time the mini-pulser produces an rf pulse it also produces a "sync" pulse. The Boxcar(PAR model 160)¹² was used in a mode where each "sync" pulse initiated a time base for the integrator. With the model 160 set on "HOLD" the integrator sampled the mini pulser output over a narrow time aperture($\sim 1 \mu\text{sec}$) at a fixed time, τ_D , after each "sync" pulse. The output of the boxcar was then proportional to the average voltage level at some fixed time after the rf pulse ($\tau_D > \text{pulse width}$). The various time bases and voltages are shown in Figure 2.

The boxcar output was displayed on the Y axis and a Hall probe output, proportional to the applied field, was displayed on the X axis of an X-Y recorder. Figure 3 shows a sample recording made using this technique. The field at which zero beats occurred for each of the five ^{127}I resonances is marked

by an arrow. Several unresolved proton resonances are also seen between 2 and 3 kOe.

D. Crystal Orientation

All three crystals exhibited well developed faces with consistent morphology. Orientation was done by optical goniometry or simply by looking at the faces. As a check on the morphologies, at least one sample of each salt was checked by X-ray crystallography to confirm the correct labeling of axes.

III. $((\text{CH}_3)_3\text{NH})\text{CuCl}_3 \cdot 2\text{H}_2\text{O}$ -

A TWO DIMENSIONAL SQUARE

HEISENBERG FERROMAGNET

A. Crystal Structure and Preparation

The crystal structure and some magnetic properties of $((\text{CH}_3)_3\text{NH})\text{CuCl}_3 \cdot 2\text{H}_2\text{O}$ have recently been reported by Losee et. al.¹³ The compound is monoclinic and belongs to the space group $P2_1/c$ with $a=7.479 \text{ \AA}$, $b=7.864 \text{ \AA}$, $c=16.730 \text{ \AA}$, and $\beta=91.28^\circ$ with four chemical-formula units per unit cell. The most significant feature of the structure is the chains of edge-sharing $\text{CuCl}_4(\text{OH}_2)_2$ octahedra running along the a-axis. These chains may be pictured as bonded into layers of composition $\text{CuCl}_3 \cdot 2\text{H}_2\text{O}$ situated at heights 0 and 1/2 along the c-axis. These layers are separated by layers composed of $(\text{CH}_3)_3\text{NH}$.

The properties of the analogous cobalt salt have been well explained using a two-dimensional rectangular Ising model. Although the cobalt salt is orthorhombic and the copper is monoclinic, the monoclinic salt can be derived from the orthorhombic by a 2° macroscopic distortion. Thus the description of their microscopic properties may be similar.

Green single crystals were grown from a 1:1 mixture of $((\text{CH}_3)_3\text{NH})\text{Cl}$ and $\text{CuCl}_2 \cdot 2\text{H}_2\text{O}$ in water at room temperature. Following the convention of Losee et.al.¹², the a and c axes have been interchanged relative to Groth's morphological description¹⁴.

Figure 4. Angle dependence of the ESR of $((\text{CH}_3)_3\text{NH})\text{CuCl}_3 \cdot 2\text{H}_2\text{O}$ in the ac' plane plotted as g^2 vs. θ . The curves are the least squares result used in the principal axis determination.

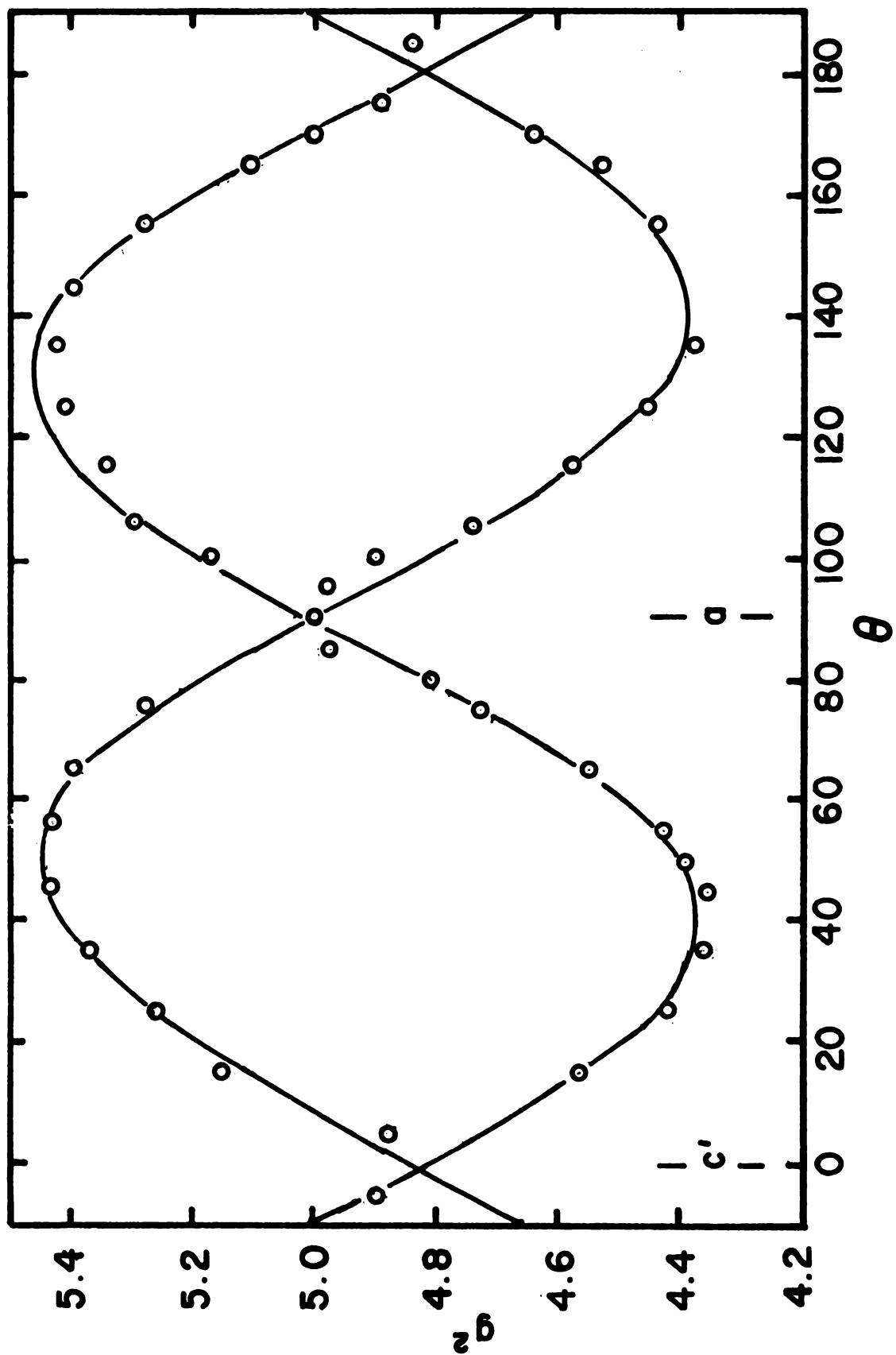


Figure 4

B. Experimental Results

In order to confirm low-dimensional behavior as suggested by Losee et.al¹³, magnetic susceptibility was measured down to .025 K. This permitted determination of the ordering temperature as well. In addition ESR measurements were made in the paramagnetic state at T=300, 77, and 4 K.

1. ESR - Principal Axis Determination

Although this is a magnetically concentrated salt, the ESR lines at 77 K were only 250 Oe wide, so that the signals from nonequivalent coppers were resolvable and g-value accuracy of 1/2% could be obtained.

The principal g values and axis orientations relative to the crystal were determined from measurements of the g-value variation in the ab, bc', and c'a planes. The c' axis is defined as the axis perpendicular to the ab plane. It differs from the c-axis by less than 2°. Using the method of Schonland¹⁵, these rotation patterns were fit by a least squares technique to

$$g^2 = \alpha + \beta \cos 2\theta + \gamma \sin 2\theta \quad (3.1)$$

Figure 4 shows the rotation pattern for g^2 in the ac' plane and the resulting fit. From α , β , and γ determined for each rotation, the g-tensor elements were determined. The principal values were obtained by diagonalizing this tensor. There are four chemical-formula units, and therefore four copper atoms per unit cell, but no more than two resonance lines were observed in any rotation. Thus only two

nonequivalent paramagnetic complexes could be resolved. The observed rotation patterns correspond to two principal-axis g-tensors having essentially the same principal values but different principal axes. The principal values and polar and azimuthal angles specifying these two tensors are given in Table I. Although the principal axes do not coincide with the crystal axes, the g-values parallel to the crystal axes are well determined, being the g-value extremes in the ab rotation, where only one resonance line was observed, and the values where the two observed lines cross for the other two rotations. Near the crossing where two lines overlap, the absorption maxima were not resolved so that the fit to the rotation patterns gives a better determination of the crystal axes g-values than a single measurement on each axis. The values obtained are $g_a = 2.238 \pm 0.010$, $g_b = 2.037 \pm 0.010$, and $g_c = 2.195 \pm 0.010$.

The data used in this determination was taken at $T = 77$ K, but no difference in the rotation patterns was observed in data taken at 300 and 4 K except for a signal to noise enhancement at lower temperatures.

2. Magnetic Susceptibility

The magnetic susceptibility data is displayed in Figure 5 where χ^{-1} is plotted for the a, b, and c axes over the entire temperature range for which data was taken. In Figure 6 the magnetic susceptibility, χ , parallel to these three axes at temperatures below 0.45 K is shown.

Table I

Principal g-tensor Values and Orientations

θ is measured from the c' axis toward the ab plane and ϕ is measured from the a -axis toward the b -axis.

Tensor 1

g	θ	ϕ
2.343 \pm .010	49.8 \pm 2.0	170.1 \pm 2.0
2.027 \pm .010	74.4	273.6
2.095 \pm .010	44.4	20.3

Tensor 2

g	θ	ϕ
2.333 \pm .010	140.5	176.9
2.029 \pm .010	76.9	103.7
2.101 \pm .010	42.4	151.6

Figure 5. Inverse magnetic susceptibilities of $((\text{CH}_3)_3\text{NH})\text{CuCl}_3 \cdot 2\text{H}_2\text{O}$ measured parallel to the a, b, and c axes.

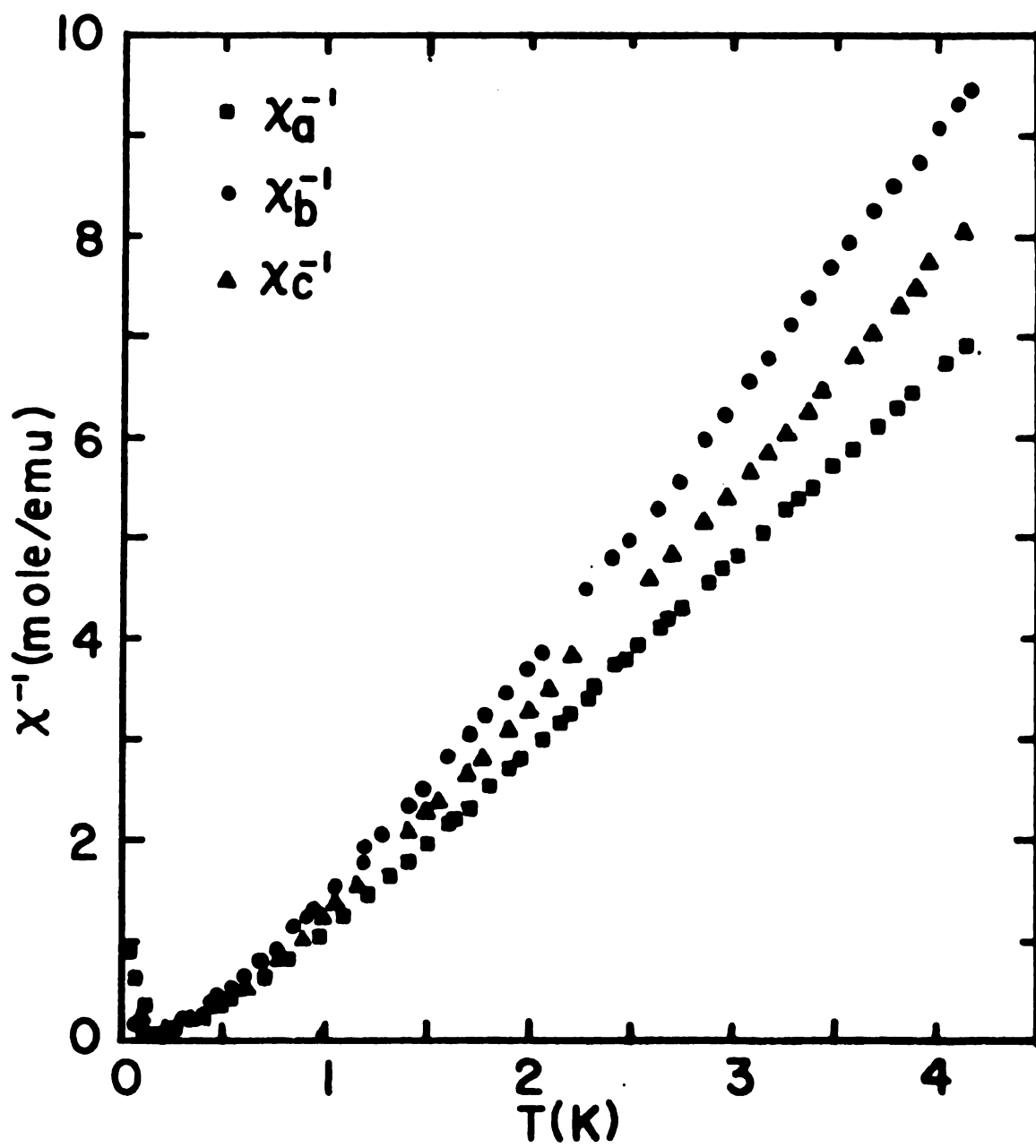


Figure 5

Figure 6. Magnetic susceptibilities of $((\text{CH}_3)_3\text{NH})\text{CuCl}_3 \cdot 2\text{H}_2\text{O}$ measured parallel to the a, b, and c axes near the transition temperature.

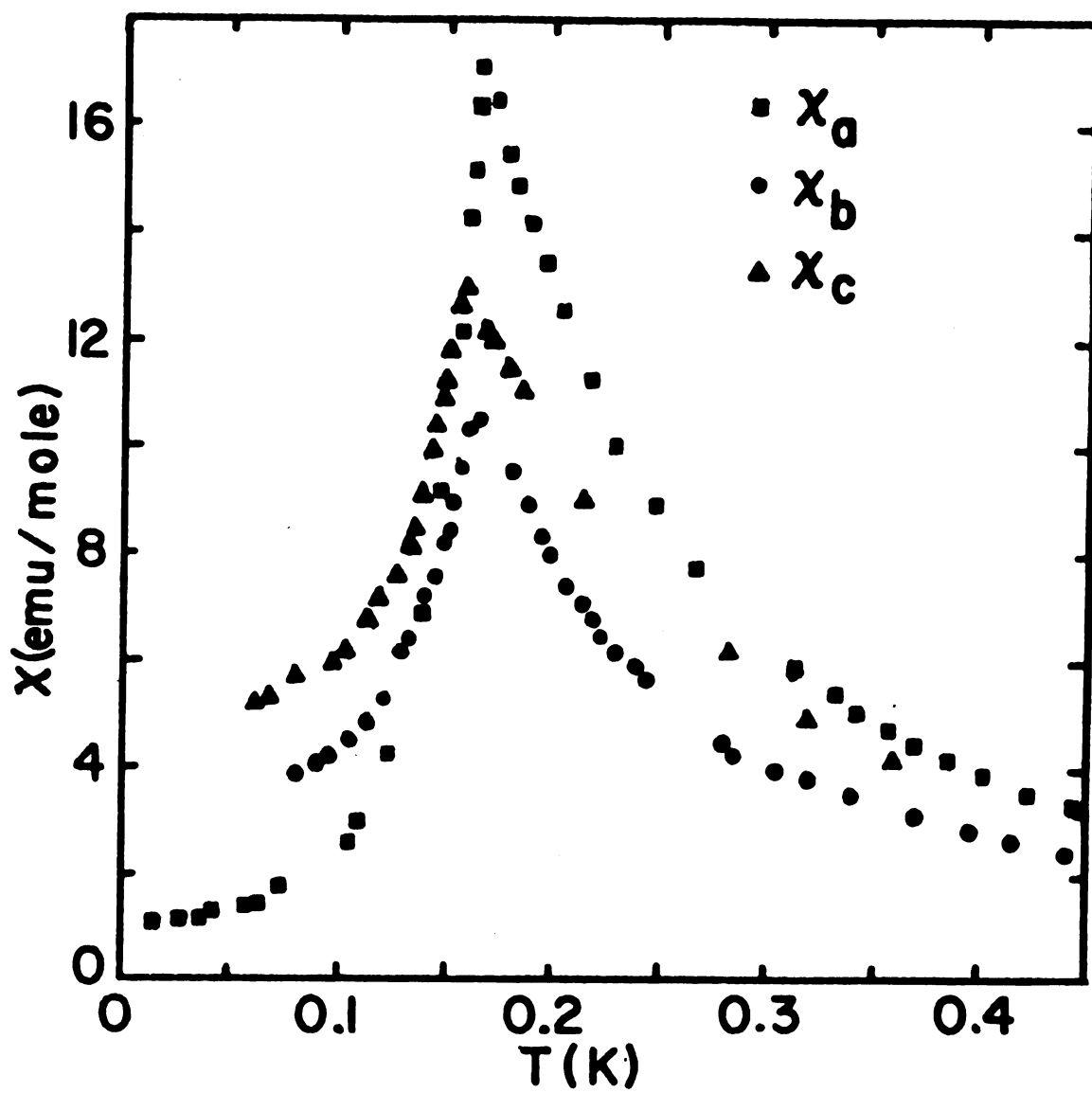


Figure 6

There are three interesting features in the results. First, the system does order magnetically at $T_c = 0.157 \pm 0.003$ K, where the ordering temperature is taken as the point of maximum $d\chi_a/dT$. Second, the behavior of χ well below T_c appears to be antiferromagnetic in nature, yet χ_a , which most resembles $\chi_{||}$, does have a nonzero value as $T \rightarrow 0$. Experimental errors due to misalignment and empty-sample-holder contributions are smaller than this deviation. In addition, χ_b and χ_c exhibit strong temperature dependence below T_c , unlike χ_{\perp} for an antiferromagnet. The third feature is the large value of the peak susceptibility for all three axes. Such a large peak in the susceptibility could arise from antiferromagnetic order with the spins canted away from an antiparallel alignment; or it could be the result of ferromagnetic planes weakly coupled antiferromagnetically.

C. Interpretation of Results

The ESR results do not lend themselves to a simple interpretation. Attempts at relating the principal axes orientations to the Cu-Cl and Cu-O directions of the distorted octahedron surrounding the coppers were not successful.

The angle dependence of the line widths was compared with the Dietz et.al.¹⁶ result for exchange narrowing in a one dimensional system, and no correlation was found.

The main value of the ESR results is in the determination of g values to be used to calculate Curie constants for the susceptibility. In addition, the presence of two

different g tensors provides a possible explanation for the behavior of χ in the ordered state.

The susceptibility results above 1.5 K show no unusual behavior. Thus Losee et.al.¹³ found they could fit both their susceptibility and specific heat results to a variety of models with no conclusive results. They fit their results to Curie-Weiss, Ising linear chain, and isotropic Heisenberg ferromagnetic chain models.

The data in Figure 5 shows that χ^{-1} varies from linear Curie-Weiss behavior below 1 K. Fitting χ in this temperature region should distinguish between various models.

The cobalt salt^{1,2} is best described as an Ising lattice with $J_1/k=7.7$ K, $J_2/k=0.09$ K, and $J_3=-.01$ K giving rise to ferromagnetic sheets very weakly coupled antiferromagnetically with a net moment. (See Section IV) The lack of deviations from Curie-Weiss behavior above 1 K for the copper salt indicates that J_1 is much smaller than it was in the cobalt salt. Since copper has rather small g -factor anisotropy, and (being $S=1/2$) no zero field splitting, it is unlikely to be Ising-like.

In the light of these factors a fit of the susceptibility data above T_c to a two-dimensional ferromagnetic Heisenberg model with an anisotropic g -tensor was performed. Since there are no exact solutions available, the high temperature series expansion, due to Baker et.al.¹⁷, for a square lattice was used. In order to best display deviations from Curie-Weiss behavior one normally plots $C/\chi T$ vs. J/kT . Figure 7 is a

Figure 7. The magnetic susceptibility of $((\text{CH}_3)_3\text{NH})\text{CuCl}_3 \cdot 2\text{H}_2\text{O}$ measured parallel to the c-axis plotted as $C/\chi T$ vs. J/kT . Solid curve (1) is the Curie-Weiss result with $\theta = 2J/k$, (2) is the square Heisenberg ferromagnet, and (3) is the Heisenberg ferromagnetic chain (abscissa scaled down by a factor of 2). ($J/kT = 0.5$ corresponds to $T = 0.56$ K)

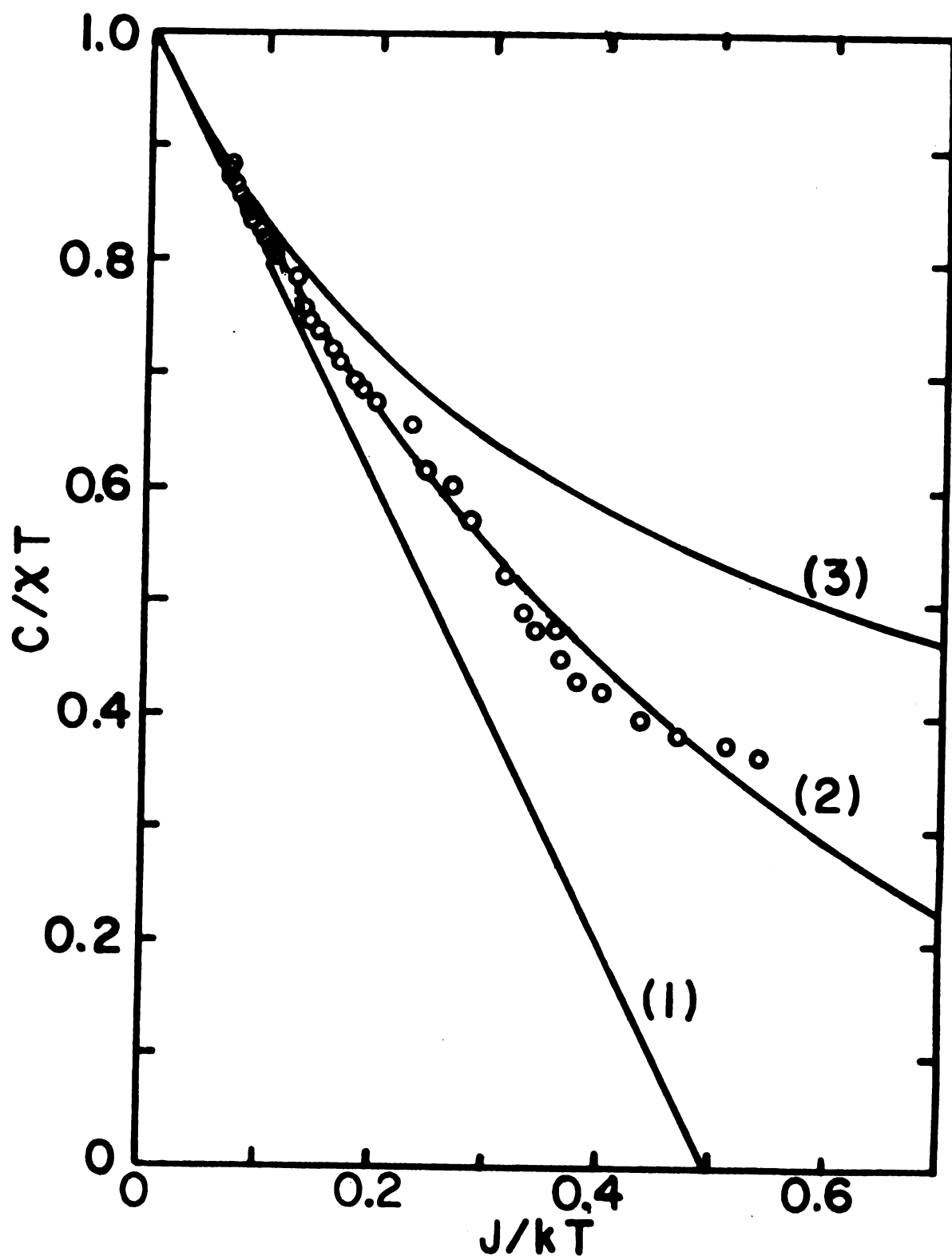


Figure 7

graph of $C/\chi_c T$ vs. J/kT , where C is calculated from $C = N_0 g_c^2 \mu_B^2 S(S+1)/3k$ using $S=1/2$ and g_c from the ESR results. The solid line (2) is obtained using the first ten terms of Baker's expansion. The best fit is obtained for $J_1/k = J_2/k = 0.28 \pm 0.02$ K. For comparison, curve (1) is the Curie-Weiss law with $\theta = 2ZJS(S+1)/3k$, which reduces to $(C/\chi T) = (1 - 2J/kT)$ for the two-dimensional square lattice; and curve (3) is the Bonner and Fisher¹⁸ result for a Heisenberg linear chain with $S=1/2$. Note that the abscissa for the Bonner and Fisher¹⁸ result has been scaled down by a factor of 2. There is no value of J/k for which either of these expressions gives as good an overall fit as does the two-dimensional square ferromagnetic Heisenberg interaction. The b-axis data is fit equally well using g_b from the ESR results with the same value of J/k .

The interpretation of χ_a is not as simple. Using the value of $g_a = 2.24$ found by ESR, no value of J/k gives anything resembling a fit to any of the proposed models. However, if we make a two parameter fit to the square Heisenberg lattice high temperature expansion allowing g and J/k to vary, a fit comparable to that obtained for the b and c axes is obtained. This fit corresponds to $g_a = 2.36 \pm 0.02$ and $J/k = 0.28 \pm 0.02$ K. It is striking that although there is a discrepancy between the ESR and susceptibility g values, the same J values are obtained from all three fits. None of the models considered offered any resolution of this discrepancy in the value of g_a .

The susceptibility results above the transition

temperature indicate that trimethylamine copper chloride behaves as a two-dimensional Heisenberg ferromagnet. Fitting the results to a square lattice in which $J/kT=0.28$ K may well be an over-simplification, since a rectangular lattice with two different exchange interactions would no doubt be more realistic, but this problem has not been solved. Below T_c , the data seems to indicate that the ferromagnetic sheets are antiferromagnetically ordered with successive ab planes oriented oppositely. The antiferromagnetic interaction may arise from dipole-dipole interactions or from a weak exchange interaction. In any event, the interlayer interaction, J_3 , will be denoted by J_{AF} and the intralayer ferromagnetic interaction, $J_1=J_2$, by J_F .

The properties of a layered structure with ferromagnetic intralayer exchange and a weaker antiferromagnetic interlayer coupling have been studied by a number of authors¹⁹⁻²³; both theoretically, using a variety of two sublattice models, and experimentally. Attempts have been made to apply several of these models to the experimental results.

The success of Berger and Freidberg²² in fitting χ vs. T for the layered structure, $Ni(NO_3)_2 \cdot 2H_2O$, using a simple molecular field calculation suggested such a calculation might describe the ordered state susceptibility of $((CH_3)NH)CuCl_3 \cdot 2H_2O$. No meaningful results were obtained using this approach.

From measurements made on several metallo-organic salts exhibiting two-dimensional ferromagnetic Heisenberg behavior, de Jongh et.al.²³ have drawn a series of empirical conclusions concerning the magnetic properties of such salts. They

define T'_C to be the temperature at which χ for such a two dimensional lattice diverges. They observe that above T'_C χ drops steeply. They deduce that the relationship between T'_C and J_F is $kT'_C/J_F \sim 0.44$. In one compound, $(C_2H_5NH_3)_2CuCl_4$, they observed the effect of a weak antiferromagnetic coupling between the layers. In this compound three dimensional order occurred at a temperature, T_C , approximately 25% greater than T'_C determined from J_F . Also they found that $\chi_{||}$ dropped steeply on both sides of T_C from a large peak value given by $\chi_{||max} T_C/C \sim 85$. χ_{\perp} showed only slight temperature dependence below T_C . They concluded that the effect of J_{AF} is to shift the ordering temperature up from T'_C determined by J_F , and to cause $\chi_{||}$ to fall steeply below T_C . They also conclude that the ferromagnetic layers explain the large peak value and the steep fall of χ above T_C . Inserting $J_F/k=0.28$ K into the expression they deduced for T'_C gives $T'_C \sim 0.12$ K. The ordering temperature for $((CH_3)_3NH)CuCl_3 \cdot 2H_2O$, $T_C=0.157$ K, is approximately 25% greater than T'_C . $\chi_{max} T_C/C \sim 5$ for this salt is much less than that for $(C_2H_5NH_3)_2CuCl_4$, but it is still larger than the molecular field prediction, $\chi_{max} T_N/C=1$. Thus the behavior of χ agrees with the empirical results de Jongh et.al.²³ deduced for a two dimensional Heisenberg ferromagnet with weak antiferromagnetic interplanar coupling.

As noted previously, the susceptibility in the a direction, which we would like to associate with $\chi_{||}$, has a nonzero value as $T \rightarrow 0$. This could be due to canting of spins on inequivalent ions. Spin resonance results indicate there are

two anisotropic g-tensor orientations for the copper ion sites. Silvera et.al.²⁴ have shown that two anisotropic g-tensors tilted with respect to each other are sufficient to produce canting of the spins on the inequivalent sites, even with isotropic exchange. Assume as a first approximation that tensor 2 can be obtained from 1 by a rotation of 2θ around the b-axis, as in Figure 8. The x, y, z coordinate system is the crystal system and x'_i, y'_i, z'_i coincide with the principal axes of the i^{th} g-tensor. In order to consider anisotropic effects due to the g tensors the exchange is described as an isotropic exchange between two "true" spins.

$$\mathcal{H} = -2J_F \vec{S}_1 \cdot \vec{S}_2 \quad (3.2)$$

Although the exchange written in this form is isotropic, the true spin magnitudes will be anisotropic if the ions' environment is a distorted octahedron. The problem is handled more simply by using isotropic effective spin variables \vec{s}_1 and \vec{s}_2 , and including the anisotropy in effective exchange constants. In the case of Cu^{++} the orbital contribution is zero to first order and the anisotropic g values relate the true spin components to the effective spin components in the principal axis coordinate system as

$$S_i = g_i s_i / 2 \quad (3.3)$$

where $i=x', y', z'$. Referring to Figure 8, the Hamiltonian, equation (3.2), can be written in terms of the effective spins as

Figure 8. The various coordinate systems used to show canting due to g-tensor inequivalence. xyz is the crystal system; $x'y'z'$ is the system in which the g-tensor is diagonal; $x''y''z''$ is the system in which \vec{s} lies along y'' in equilibrium.

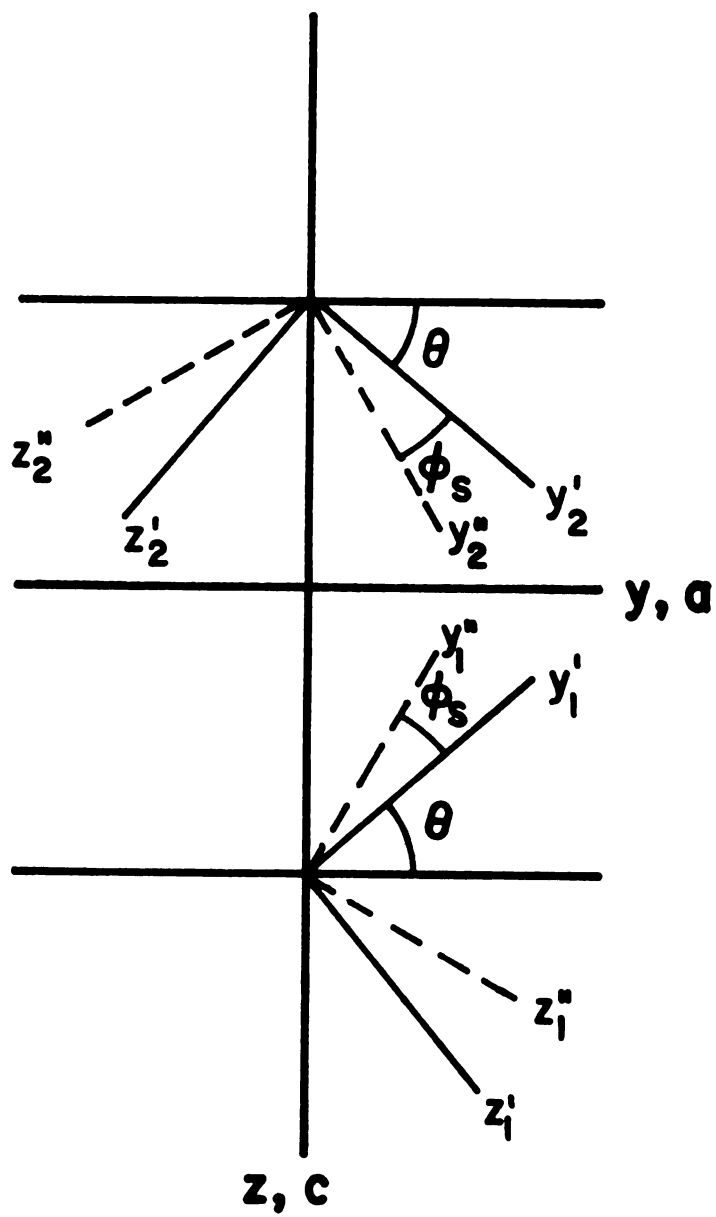


Figure 8

$$\begin{aligned}
\mathcal{H} = & -J[(g_x')^2 s_{1x'} s_{2x'} + (g_y')^2 \cos 2\theta s_{1y'} s_{2y'} \\
& + (g_z')^2 \cos 2\theta s_{1z'} s_{2z'} \\
& - g_y' g_z' \sin 2\theta (s_{1y'} s_{2z'} - s_{1z'} s_{2y'})]
\end{aligned} \tag{3.4}$$

Thus the symmetric elements of the effective exchange dyadic (See Section I) are

$$\begin{aligned}
J_{x'x'} &= -(g_x')^2 J \\
J_{y'y'} &= -(g_y')^2 J \cos 2\theta \\
J_{z'z'} &= -(g_z')^2 J \cos 2\theta
\end{aligned} \tag{3.5}$$

and the nonzero antisymmetric elements are

$$J_{y'z'} = J_{z'y'} = g_y' g_z' J \sin 2\theta \tag{3.6}$$

It is this antisymmetric exchange which leads to a canting of the effective spins. Silvera et.al.²⁴ then define the x''_i, y''_i, z''_i coordinate axes, such that in equilibrium $\langle \vec{s}_1 \rangle$ and $\langle \vec{s}_2 \rangle$ are parallel to y''_1 and y''_2 . In this frame $s_{y''}$ is a constant of the motion, therefore

$$i\hbar ds_{y''}/dt = [s_{y''}, \mathcal{H}] = 0 \tag{3.7}$$

Solving this for the equilibrium angle, ϕ_s , \vec{s} makes with the y' axis gives

$$\tan 2\phi_s = \frac{-2g_y' g_z' \tan 2\theta}{(g_y')^2 + (g_z')^2} \tag{3.8}$$

or in terms of the effective exchange constants,

$$\tan 2\phi_s = \frac{2J_{y'z'}}{J_{y'y'} + J_{z'z'}} \tag{3.9}$$

Figure 9. The relationship between the effective spin \vec{s}_1 and magnetic moment \vec{m}_1 .

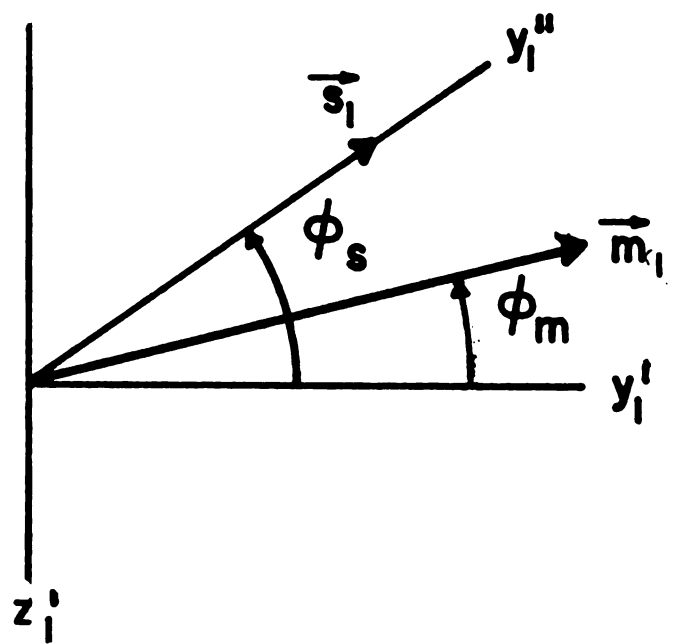


Figure 9

The values obtained from the principal axes determination, $g_{y'}=2.34$, $g_{z'}=2.10$ and $\theta \sim 40^\circ$, gives

$$\phi_s = -39.97^\circ$$

Therefore, the effective spins are canted less than $.1^\circ$ from the y (i.e. a) axis. The quantity of real interest, however, is the orientation of the magnetic moment. Defining the angle between the magnetic moment equilibrium position and the y' axis, ϕ_m , the situation for spin 1 is shown in Figure 9. Since $\vec{m} = \mu_B \vec{g} \cdot \vec{S}$ it follows that

$$\tan \phi_m = \frac{g_{z'}}{g_{y'}} \tan \phi_s \quad (3.10)$$

Substituting the appropriate values one obtains $\phi_m = -37^\circ$. The canting angle of the moment relative to the y axis is given by $\theta + \phi_m$. Therefore moment 1 is canted 3° from a towards $(-c')$ while moment 2 is canted 3° towards $+c'$.

Although the rotational inequivalence of the two tensors is more complicated than assumed above, the conclusion that the magnetic moments are canted a few degrees from the a -axis is probably valid. Other factors such as anisotropic exchange may contribute to the canting, but canting is a probable explanation for the nonzero value of χ_a as $T \rightarrow 0$.

Canting also explains the strong temperature dependence of χ_b and χ_c below T_c . An upper limit on the magnitude of J_{AF} can be obtained by assuming that the value of χ_b and χ_c extrapolated to $T=0$ is given by the molecular field expression for χ_\perp of a two sublattice layered antiferromagnet²³.

$$\chi_{\perp} = \frac{Ng\mu_B S}{2H_{AF}} = \frac{Ng^2\mu_B^2}{2zJ_{AF}} \quad (3.11)$$

Using χ_c extrapolated to zero and $z=2$ one obtains $J_{AF}/k \sim -0.023$ K. This is an upper limit on the magnitude of J_{AF} since $\chi_c(T \rightarrow 0)$ will be less than the molecular field prediction if canting is present. Therefore the magnitude of the intraplanar exchange is at least a factor of 10 greater than the interplanar exchange.

The probable ordered state spin configuration is shown in Figure 10. The spins lie in the ac plane mostly along a . Successive spins along a are canted towards c and $-c$. Spins in adjacent ab planes are antiparallel.

There are five members of the family²⁵ of magnetic space groups belonging to $P2_1/c$. Since the copper atoms are located at inversion centers in $P2_1/c$, and since no magnetic moment can exist at an antiinversion center, the two members containing anti-centers can be eliminated. The three remaining groups are $P_{2a}2_1/c$, P_a2_1/c , and $P2'_1/c'$. If the group were $P2'_1/c'$ then the a component of all spins would be equal and parallel. The assumption that the a components of spins on successive layers are antiparallel eliminates this group. $P_{2a}2_1/c$, obtained by doubling the unit cell along a , is possible but not necessary to explain the observed data. Thus the probable magnetic space group is P_a2_1/c which is consistent with Figure 10.

In conclusion, $((CH_3)_3NH)CuCl_3 \cdot 2H_2O$ displays the properties of a two-dimensional Heisenberg ferromagnet above

Figure 10. Proposed ordered state spin arrangement for $((\text{CH}_3)_3\text{NH})\text{CuCl}_3 \cdot 2\text{H}_2\text{O}$. The spins lie in the ac plane.

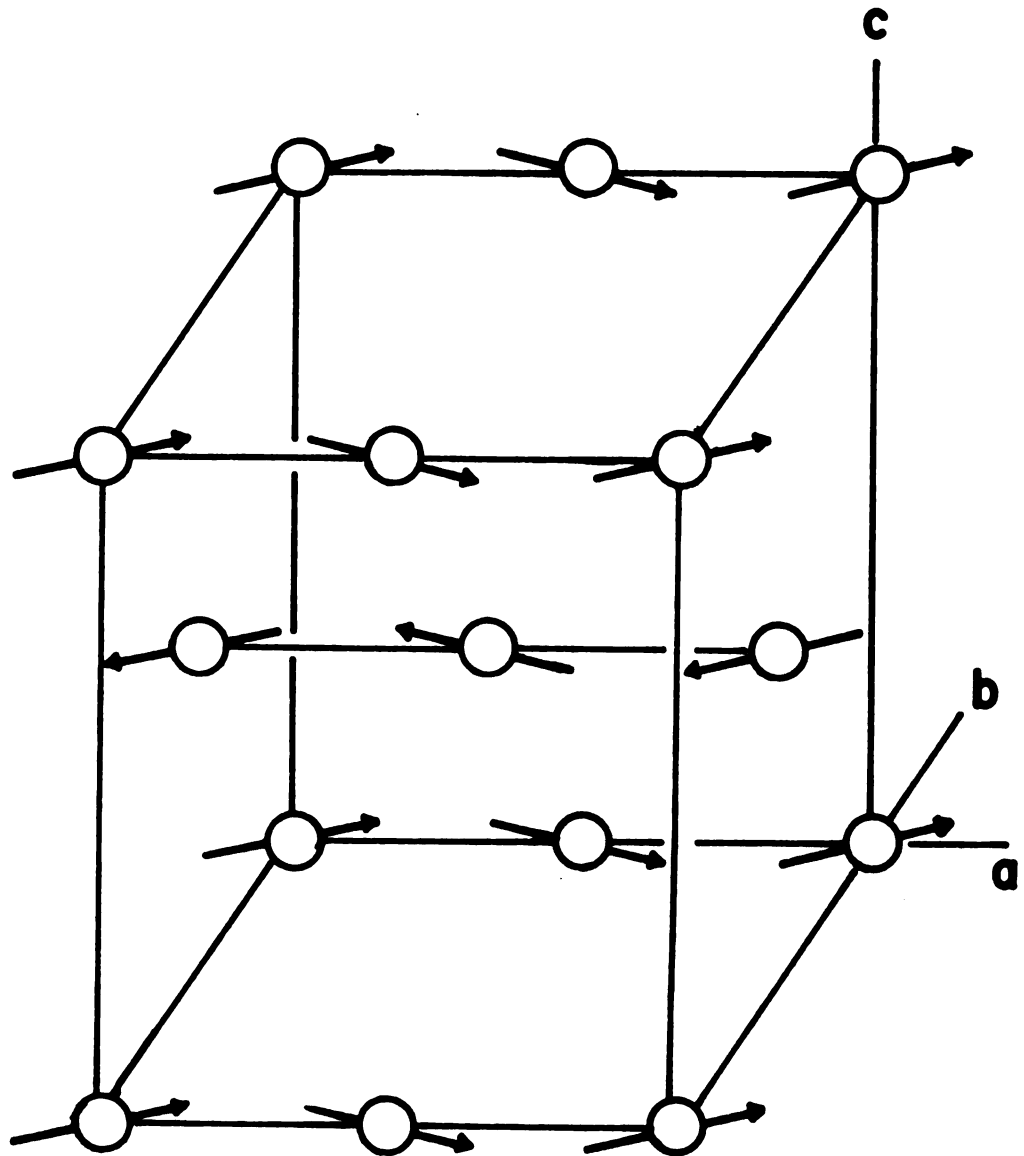


Figure 10

$T_c = 0.157$ K with $J_F/k = 0.20$ K. Below T_c it exhibits behavior characteristic of antiferromagnetic coupling between the ferromagnetic layers with $J_{AF} \sim -0.023$ K. Apparently the spins are canted slightly away from the a axis in the ordered state. The configuration has no net moment and corresponds to the magnetic space group $P_a 2_1/c$.

IV. $((\text{CH}_3)_3\text{NH})\text{CoCl}_3 \cdot 2\text{H}_2\text{O}$ - METAMAGNETIC BEHAVIOR

A. Crystal Structure and Preparation

In a recently published paper, Losee et.al.¹ reported the structure of $((\text{CH}_3)_3\text{NH})\text{CoCl}_3 \cdot 2\text{H}_2\text{O}$ in addition to detailed magnetic susceptibility and specific heat measurements in zero field. The compound is orthorhombic and belongs to the space group Pnma with $a=16.67 \text{ \AA}$, $b=7.27 \text{ \AA}$, and $c=8.11 \text{ \AA}$ with four chemical formula units per unit cell. The most significant feature of the structure is the chains of edge-sharing $\text{CoCl}_4(\text{OH}_2)_2$ octahedra running along the b-axis. These chains are bonded into layers of composition $\text{CoCl}_3 \cdot 2\text{H}_2\text{O}$ situated at heights 0 and 1/2 along the a-axis. These layers are separated by layers composed of $(\text{CH}_3)_3\text{NH}$.

The structure is similar to that of the monoclinic copper salt but the axes are labeled differently.

Single crystals were grown from equimolar solutions of $((\text{CH}_3)_3\text{NH})\text{Cl}$ and $\text{CoCl}_2 \cdot 6\text{H}_2\text{O}$. The crystals are violet/red in color but appear blue when viewed along the a-axis with light polarized parallel to c. This optical dichroism aided orientation of the samples.

B. Experimental Results

Losee et.al.¹ concluded from their measurements that above $T_N=4.135 \text{ K}$ the magnetic properties could be described by a two-dimensional rectangular lattice with Ising-like

exchange. They found good agreement with such a model with $J_1/k=7.7$ K and $J_2/k=0.09$ K. Below T_N the compound ordered three dimensionally as a canted antiferromagnet. The antiferromagnetic order indicates a small negative value for J_3 .

From the crystal structure and their measurements Losee et.al.¹ proposed a spin arrangement for the ordered state. Spence and Botterman² were able to confirm this arrangement using NMR and found that it could be described by the magnetic space group $Pnm'a'$. In this configuration the spins lie nearly parallel to c , but are canted towards the a -axis. Spence found that the application of a magnetic field greater than 64 Oe along c drastically modified the magnetization of the sample. In order to explain this metamagnetic behavior they proposed a phenomenological model. The model successfully explained the NMR and magnetization measurements. In this section measurements of the magnetic susceptibility in applied field are compared with the predictions of the model.

The model proposed by Spence and Botterman has no temperature dependence; it predicts results for the applied field only in the ac plane and only for temperatures near 2 K where they performed their NMR and magnetization experiments. Although experiments have been performed at a variety of temperatures, only the results obtained near $T=2$ K and with H in the ac plane will be discussed here. The data was normalized so that the experimental and theoretical values of χ_c were approximately equal in an applied field, $H_c=450$ Oe.

In Figure 11 the magnetic susceptibility at $T=2.05$ K

Figure 11. The field dependence of the magnetic susceptibility of $((\text{CH}_3)_3\text{NH})\text{CoCl}_3 \cdot 2\text{H}_2\text{O}$. (a) The open squares are experimental results for $\text{H} \parallel \text{c}$. The solid line is the theoretical prediction for $\theta = 0^\circ$; the dashed line is the theoretical prediction for $\theta = 3^\circ$. (b) Data and theory for $\text{H} \parallel \text{a}$ ($\theta = 90^\circ$).

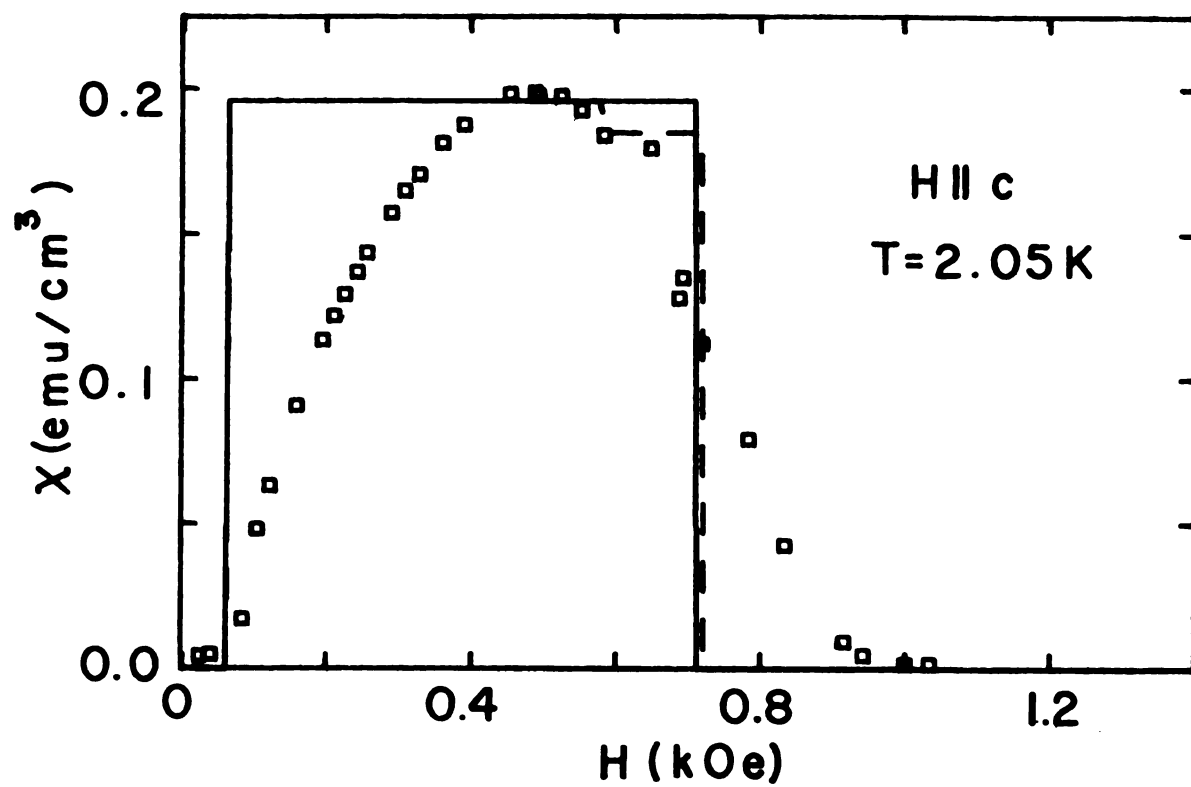


Figure 11(a)

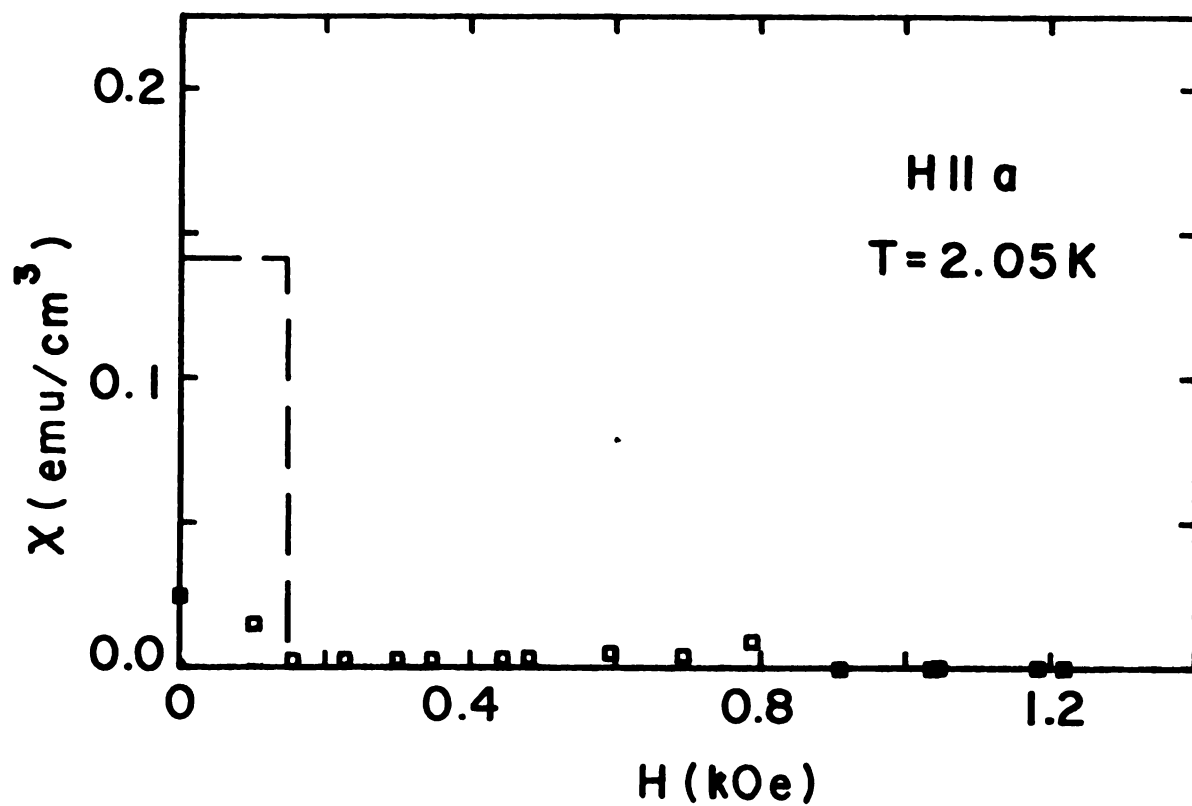


Figure 11(b)

is plotted as a function of magnetic field, H , applied parallel to the c -axis ($\theta=0^\circ$) and to the a -axis ($\theta=90^\circ$). The theoretical predictions for $\theta=0^\circ$, 3° , and 90° are also shown. The data is plotted only for fields up to 1400 Oe since for higher fields the susceptibility is approximately zero.

The rotation data taken at $T=2.32$ K is plotted in Figures 12-15. Each successive figure shows χ vs θ for a larger value of H than the preceding figure. In addition the theoretical fits are displayed.

C. Interpretation of Results

In order to compare the results for $\chi(H)$ with the Spence model it is necessary to summarize the model. He assumes that the sample consists of regions in which the spin orientations correspond to one of the configurations C_1 , C_2 , C_3 shown in Figure 16. It should be noted that although the model does not use an explicit Hamiltonian, this is equivalent to assuming the exchange is Ising-like; that is, the spins on a given sublattice can only point parallel or antiparallel to an axis z' . z' is approximately 10° from z toward $+x$ for one sublattice and towards $-x$ for the other. In this model saturation corresponds to the entire sample being in one of the three spin configurations. It does not refer to the rotation of spins away from z' at very high fields. Spence denotes by f_1 , f_2 , and f_3 the fractions of the total sample volume occupied by each of the corresponding spin configurations, thus

$$f_1 + f_2 + f_3 = 1 \quad (4.1)$$

Figure 12. χ vs. θ with $H=300$ Oe for $((CH_3)_3NH)CoCl_3 \cdot 2H_2O$.

Figure 13. χ vs. θ with $H=438$ Oe for $((CH_3)_3NH)CoCl_3 \cdot 2H_2O$.

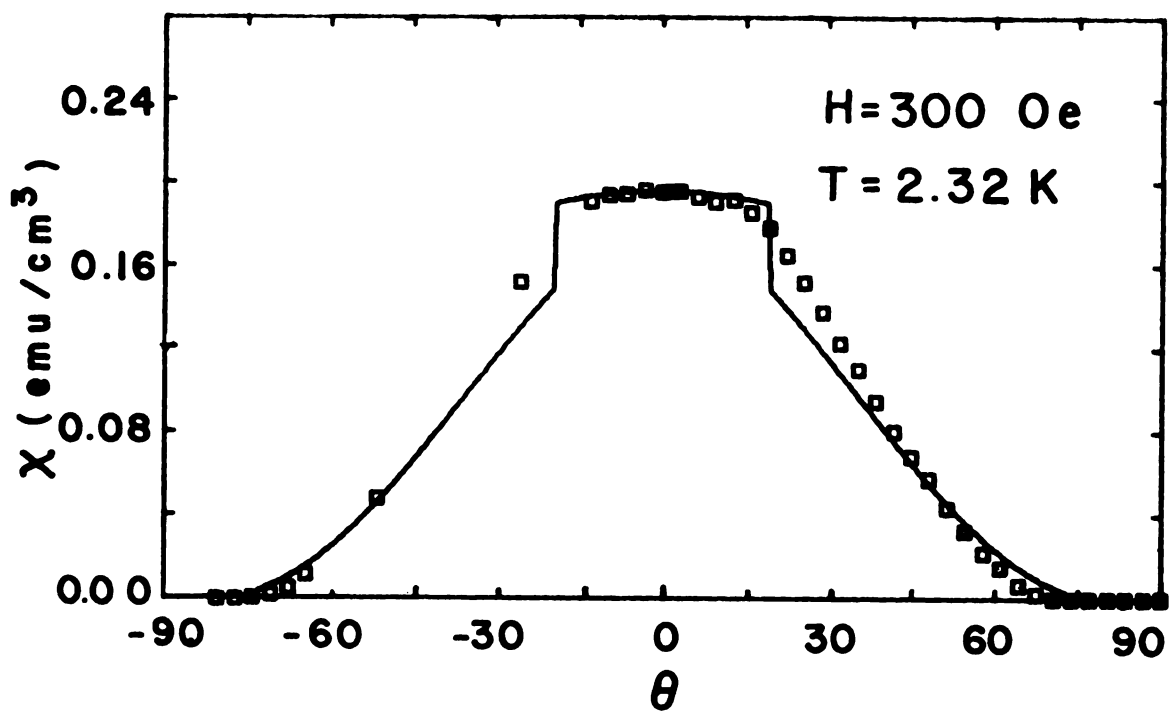


Figure 12

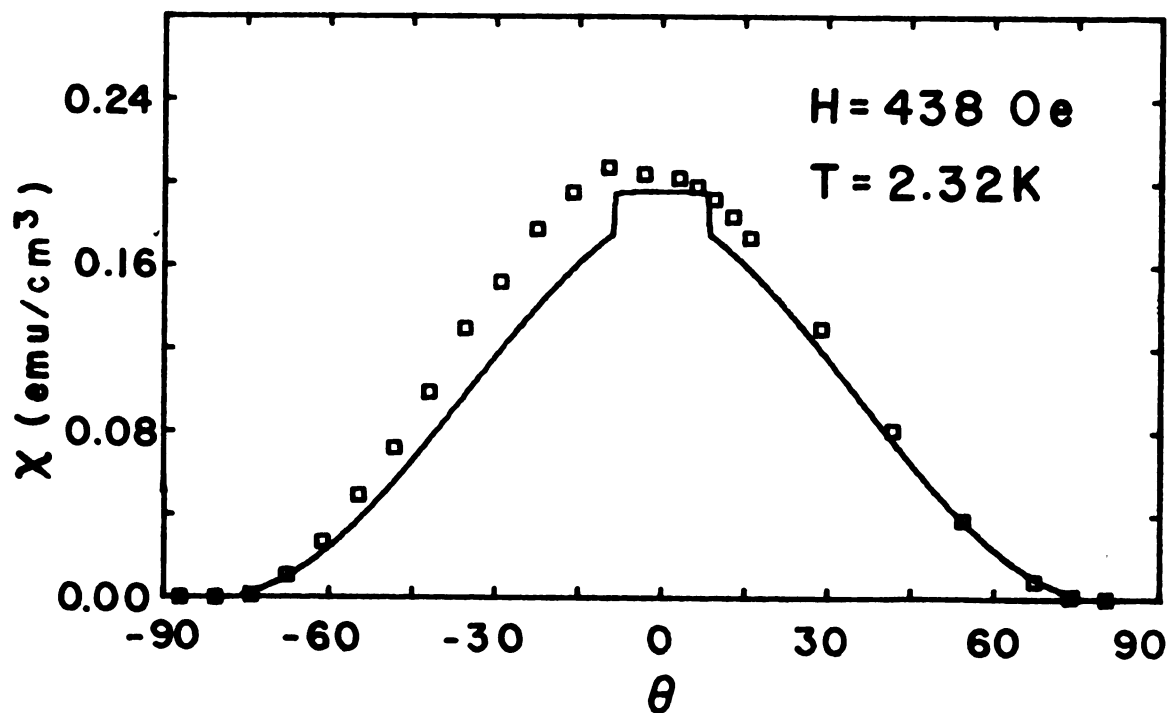


Figure 13

Figure 14. χ vs. θ with $H=976$ Oe for $((\text{CH}_3)_3\text{NH})\text{CoCl}_3 \cdot 2\text{H}_2\text{O}$.

Figure 15. χ vs. θ with $H=1075$ Oe for $((\text{CH}_3)_3\text{NH})\text{CoCl}_3 \cdot 2\text{H}_2\text{O}$.

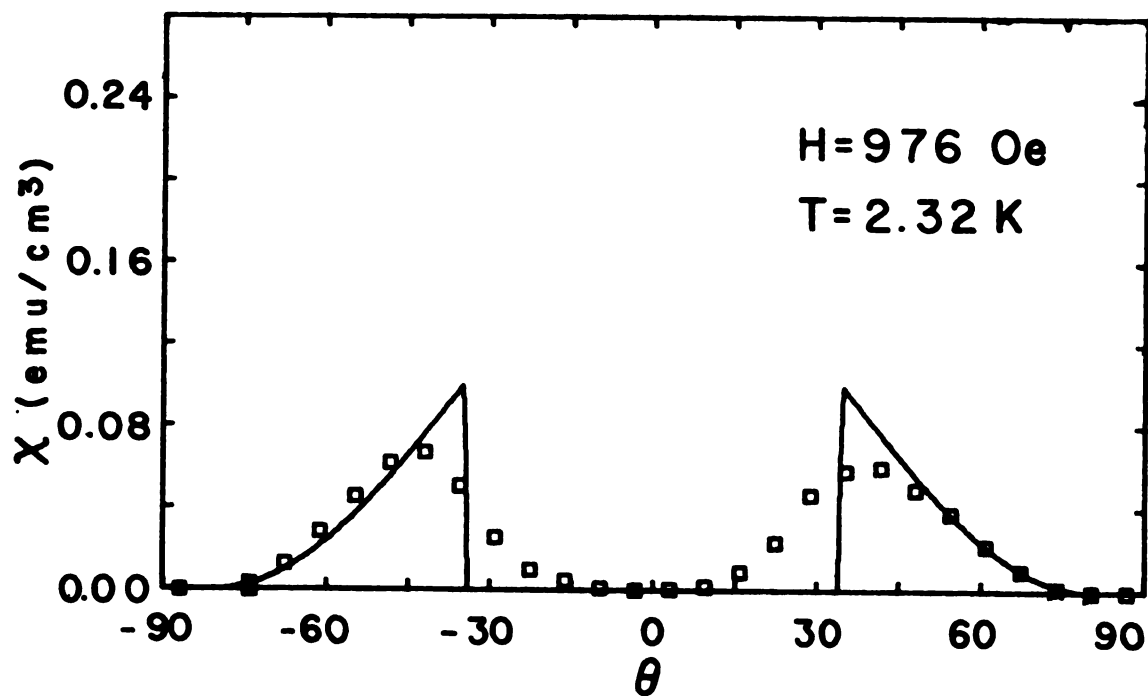


Figure 14

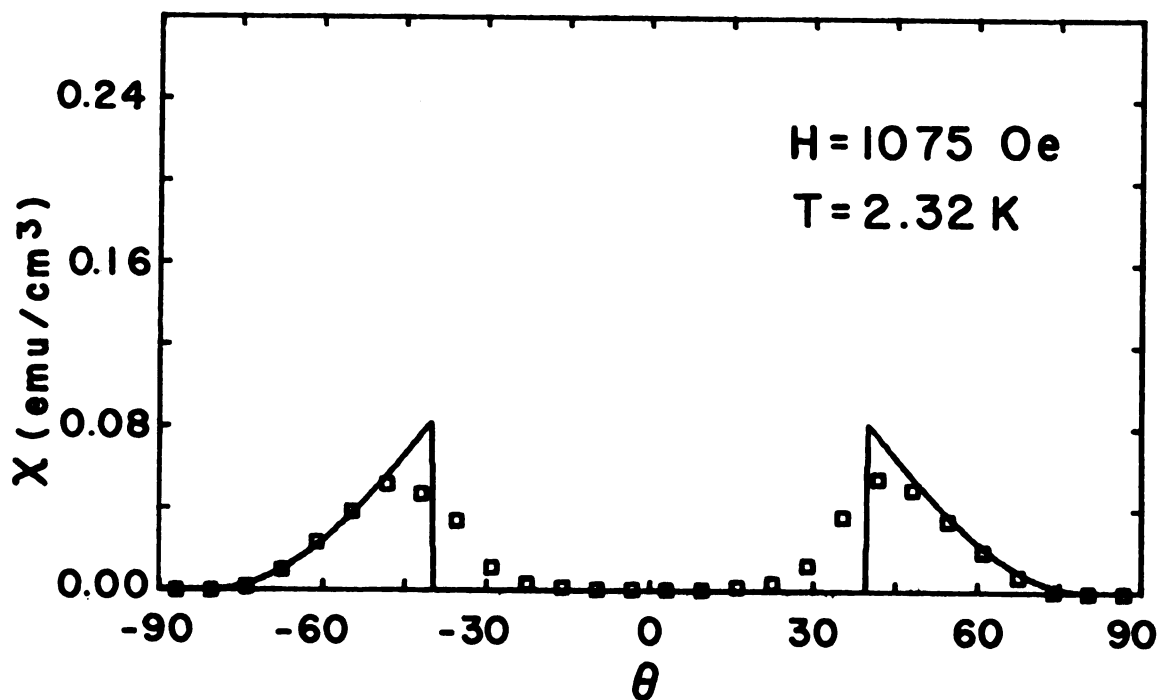


Figure 15

Figure 16. The spin configurations C_1 , C_2 , and C_3 assumed by the Spence² model.

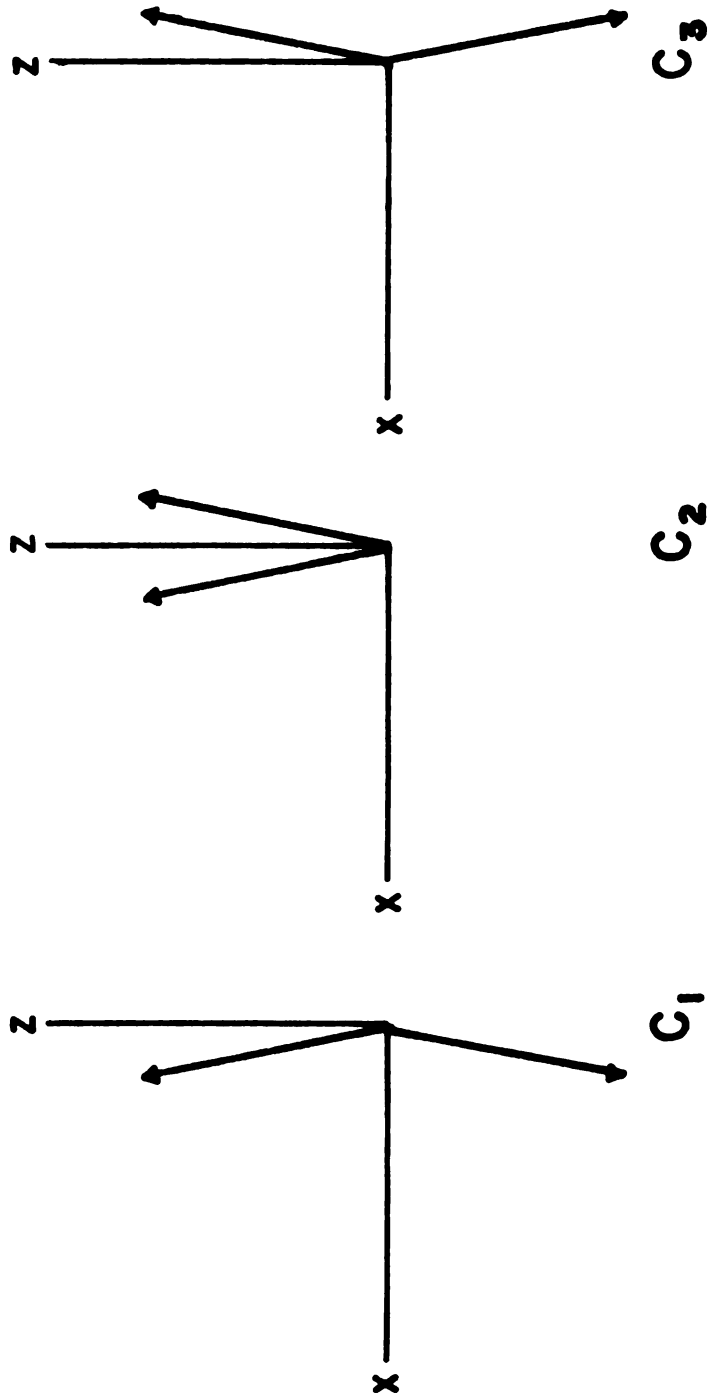


Figure 16

The magnetic energy of such a system will then be the usual magnetostatic term plus the energy to create configuration C_2 from spins in configurations C_1 and C_3 . This creation term involves the energy to overcome the weak antiferromagnetic exchange J_3 , which is characterized by a critical field, $H_k = 64$ Oe. Spence minimizes the magnetic energy subject to the restriction of equation (4.1). In order to do this he assumes a linear relation between the applied field, \vec{H} , and the internal field, \vec{H}_i , given by

$$\vec{H}_i = \vec{H} - \vec{N} \cdot \vec{M} \quad (4.2)$$

where \vec{N} is an effective demagnetizing tensor. The association of \vec{N} with the normal demagnetizing tensor²⁶ is, as Spence points out, probably invalid because the magnetization, \vec{M} , is spatially inhomogeneous. Nevertheless, such a linear relationship appears to be valid experimentally.

In order to make use of Spence's results the following definitions and assumptions are needed:

θ is the angle between applied field and c-axis,

M_x and M_z are the components of magnetization along a and c,

M_a and M_c are the saturation values of these components,

\vec{N} is diagonalized by x and z, (4.3)

N_{xx} and N_{zz} are the diagonal elements of N ,

$$H_a = N_{xx} M_a,$$

$$H_c = N_{zz} M_c,$$

$$\rho = H_a / H_c,$$

$$\zeta = M_a / M_c.$$

With these definitions and referring to Figure 16, it is clear equation (4.1) can be rewritten as

$$\frac{M_x}{M_a} + \frac{M_z}{M_c} + 2f_3 = 1 \quad (4.4)$$

Five regions of the $H-\theta$ plane can be distinguished depending on the form of equation (4.4). The components of \vec{M} for the five regions are given by:

Region A ($M_x/M_a + M_z/M_c < 1$)

$$M_x = N_{xx}^{-1} H \sin\theta \quad (4.5)$$

$$M_z = N_{zz}^{-1} (H \cos\theta - H_k)$$

Region B ($M_x/M_a + M_z/M_c = 1$)

$$M_x = N_{xx}^{-1} (1 + \zeta\rho)^{-1} [\zeta\rho H \sin\theta - \rho (H \cos\theta - H_k - H_c)] \quad (4.6)$$

$$M_z = N_{zz}^{-1} (1 + \zeta\rho)^{-1} [(H \cos\theta - H_k) - \zeta (H \sin\theta - H_a)]$$

Region α ($M_z/M_c = 1$)

$$M_x = 0 \quad (4.7)$$

$$M_z = M_c$$

Region β ($M_x/M_a = 1$)

$$M_x = M_a \quad (4.8)$$

$$M_z = 0$$

Region γ ($M_z = 0$, and $M_x/M_a < 1$)

$$M_x = N_{xx}^{-1} H \sin\theta \quad (4.9)$$

$$M_z = 0.$$

Figure 17. Regions of magnetization in the H_0 plane.

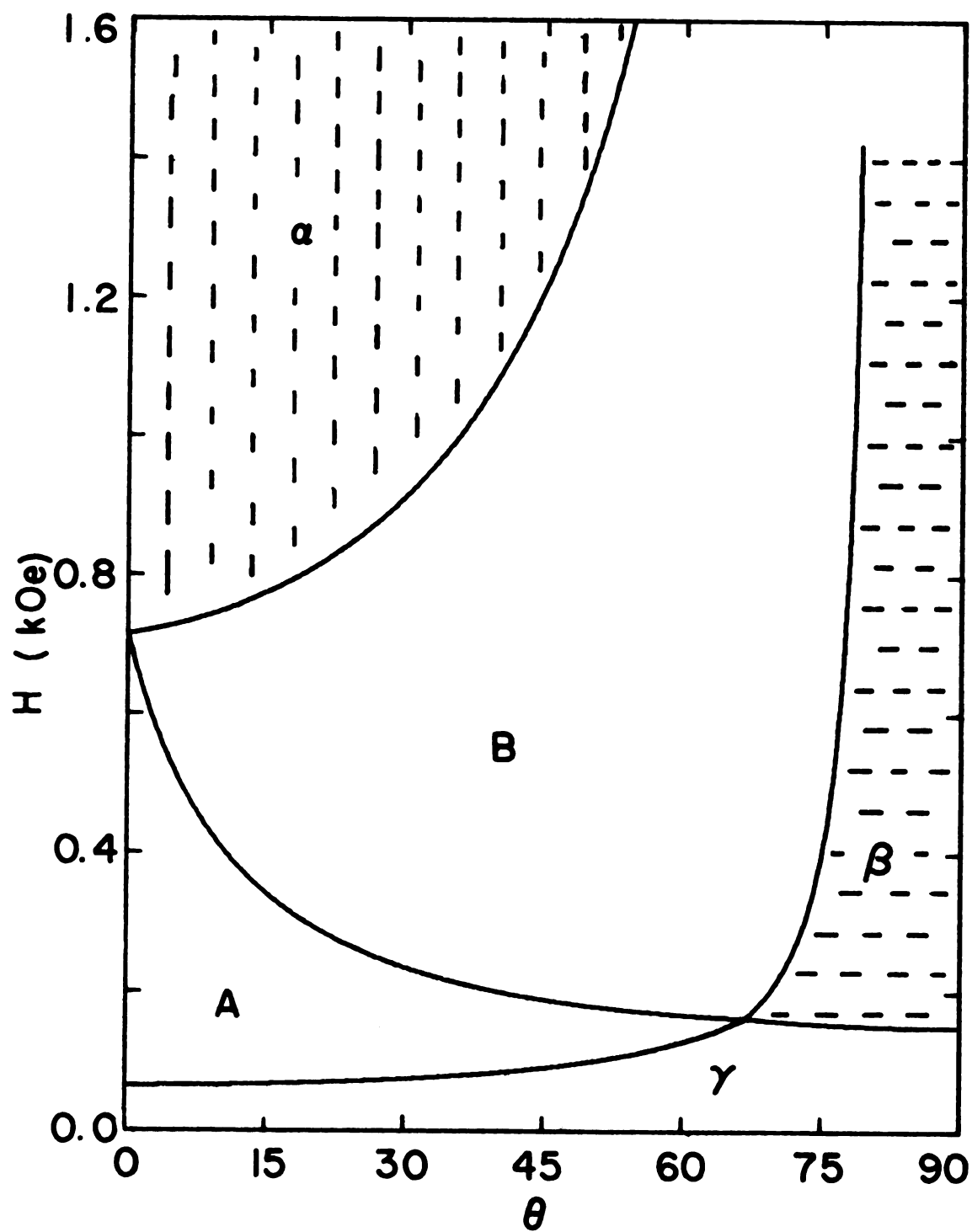


Figure 17

Regions α and β correspond to saturation of M_z and M_x .

The H - θ boundary between any two of these regions is found by determining the values of H and θ for which M_x and M_z in both regions become identical. Figure 17 shows the five regions of magnetization in the H - θ plane for the following choice of parameters: $H_k=64$ Oe, $H_a=150$ Oe, $H_c=650$ Oe, $\rho=.231$, and $\zeta=.166$.

The parameters used to fit the susceptibility data are M_a , M_c , H_k , H_a , and H_c . The critical field, H_k , is determined very accurately by NMR to be 64 Oe and since the susceptibility measurements only indicate that it is less than 100 Oe, the NMR value will be used. The saturation magnetizations are well determined from the magnetization measurements to be $M_a=21.2$ emu/cm³ and $M_c=127.4$ emu/cm³. Thus these values determined by Spence and Botterman are considered fixed and the shape dependent parameters H_a and H_c are the only parameters to be fit in this experiment.

The calculation of χ from the magnetization expression can be done numerically using,

$$\chi(H, \theta) \equiv \frac{dM_H(\theta, H)}{dH} \approx \frac{M_H(\theta, H+\Delta H) - M_H(\theta, H)}{\Delta H} \quad (4.10)$$

where ΔH is small and $M_H(\theta, H)$ is the component of $\vec{M}(\theta, H)$ parallel to \vec{H} . Then

$$M_H(\theta, H) = M_x \sin \theta + M_z \cos \theta \quad (4.11)$$

where M_x and M_z are given by the expressions for the

appropriate region of the H - θ plane.

Using such a numerical differentiation gives values of χ even at boundaries between regions where M vs H is discontinuous and χ is really undefined. The model correctly predicts χ only on either side of the boundary. A model to explain the behavior of χ at these boundaries would have to include the spin dynamics.

Since all measurements were made on a single sample, one set of shape dependent parameters, H_a and H_c , should fit the data if the model is to be further confirmed. The effect of demagnetizing factors is included in the model so normal demagnetizing corrections of the data are not necessary.

The qualitative nature of the model suggests that a quantitative fitting procedure is inappropriate. A qualitative "best fit" was found by varying the parameters to determine if an "eyeball" fit with the appropriate angle and field dependence could be found. The best values found in this manner were $H_a = 150 \pm 25$ Oe and $H_c = 650 \pm 25$ Oe. The predicted susceptibility obtained using these values is shown as the solid and dashed lines on Figure 11 and the solid lines on Figures 12-15.

The model predicts (Figure 11) that for H parallel to C ($\theta = 0^\circ$), solid line, the susceptibility is zero for $H < H_k$ (Region γ) and for $H > (H_c + H_k)$ (Region α). For $H_k < H < (H_c + H_k)$ (Region A) χ is constant at approximately 0.20 emu/cm^3 (see Figure 17). The data does not have precisely this form but χ does change sharply near these fields and reaches a large if not constant value midway between them. Qualitatively the experimental

results are as predicted except for a "rounding" of the discontinuities in χ . This "rounding" is probably related to the spins' dynamic behavior which is not included in the model. Another influence, which may be important, is the contribution to the total energy from formation and motion of domain walls.

Figure 11 also shows the prediction of χ for $\theta=3^\circ$, short dashed line, which corresponds to the maximum possible misalignment for the c-axis. Notice the lower value of χ from 590-720 Oe. This corresponds to Region B which is not encountered for $\theta=0^\circ$ (see Figure 17). The experimental data may show a slight change in this region, but such an interpretation cannot be made conclusively.

Finally Figure 11 shows the prediction for $\theta=90^\circ$, long dashed line, corresponding to H parallel to a. The qualitative behavior of the data does not as convincingly confirm the model. For $H < H_a$ the model predicts a large value of χ_a (Region γ) and it predicts $\chi_a=0$ for $H > H_a$ (Region β). The experimental susceptibility for $H > H_a$ fluctuates but is quite small and approaches zero at high fields. The low value of χ_a , compared to the model prediction, for $H < H_a$ is probably related to the temperature dependent behavior Losee et.al.¹ observed for χ_a in zero field. They observed variations from sample to sample in the temperature dependence of χ_a below T_N . With such a complicated spin structure, it is not unreasonable that the configuration of minimum energy in small fields might be sample dependent giving rise to large χ_a at $T_N/2$ for one sample and small χ_a at the same temperature for another. At

temperatures above $T=2.05$ K, χ_a for $H<100$ Oe did increase in agreement with the findings of Losee et.al. and also in better agreement with the Spence model. Thus the poor agreement for χ_a appears to be a result of the temperature independent nature of the model.

The rotation patterns, Figures 12-15, show the experimental data and theoretical predictions for $\chi(H)$ as a function of θ for four values of H . For $H_k < H < H_k + H_c$ (Figures 12 and 13) behavior characteristic of the three regions, A, B, and β , is observed. For $H > H_k + H_c$ (Figures 14 and 15) three regions, α , B, and β , are observed. The fits are only qualitatively correct but three distinct angle dependences are observed for each rotation. The distinction between regions A and α appearing as H is increased is quite striking. For completeness, note that Figure 11 shows evidence of the γ region where $\chi_c(H) \sim 0$ for $H \gtrsim 100$ Oe.

Using equations (4.3), the values of M_a and M_c given by Spence and Botterman, and the values of H_a and H_c given above, one obtains for the shape dependent demagnetizing factors $N_{xx} = 7.1 \pm 1.0$ and $N_{zz} = 5.1 \pm .2$. These values fall between the results which Spence and Botterman obtained using NMR on ellipsoidal samples and those obtained from their magnetization measurements on unshaped samples. Since the samples used for the susceptibility measurements were unshaped, these are not unreasonable values of N_{xx} and N_{zz} .

In conclusion the magnetic susceptibility measurements in applied field further confirm the validity of the

assumptions made by Spence in describing $((\text{CH}_3)_3\text{NH})\text{CoCl}_3 \cdot 2\text{H}_2\text{O}$. The model predicts qualitatively the dependence of χ on H and θ . The inclusion of temperature in a model for the behavior of this system would be interesting but difficult. If one could design such a model, experimental investigations below 2 K would be worthwhile. At present nothing is known of the spatial distribution of the various spin configurations as a function of field, orientation, and temperature, nor of domain boundary conditions. Optical and electron spin resonance experiments, in addition to further NMR, magnetization, and susceptibility experiments, might answer some of the questions.

V. $\text{NiI}_2 \cdot 6\text{H}_2\text{O}$ -
CRYSTAL FIELD SPLITTING
WITH WEAK EXCHANGE

A. Crystal Structure and Preparation

Gaudin-Louër and Weigel²⁷ have reported the X-ray determination of the unit cell parameters and Ni and I positions in $\text{NiI}_2 \cdot 6\text{H}_2\text{O}$. At room temperature the unit cell is hexagonal with $a=7.67 \text{ \AA}$ and $c=4.87 \text{ \AA}$. There is one molecule per unit cell and the density is 2.825 gm/cm^3 . The fractional coordinates are:

$$\text{Ni}^{++}: 0,0,0$$

$$\text{I}^- : 1/3, 2/3, u \text{ and } 2/3, 1/3, \bar{u}$$

where $u \approx 0.22$. The O positions were not determined but they probably form a regular octahedron about the Ni. Depending on the symmetry of this octahedron, Gaudin-Louër et.al. conclude the chemical space group is $P\bar{3}$ or $P\bar{3}n1$.

The magnetic measurements reported in this section indicate that at low temperatures there are two different Ni^{++} complexes, each having axial symmetry about the c-axis. The appearance of two different Ni environments implies that a crystallographic phase change occurs between room temperature and 4.2 K. This phase change must result in a doubling of the unit cell while the axial symmetry suggests the change may involve an axial distortion of the octahedron.

Single crystals were grown from a saturated aqueous solution of $\text{NiI}_2 \cdot 6\text{H}_2\text{O}$. The green hexagonal crystals have a

cleavage plane perpendicular to the c axis and are quite hygroscopic.

B. Experimental Results

ESR, zero-field magnetic susceptibility and NMR measurements were made to study the relative magnitudes of crystal field splitting and magnetic exchange in nickel iodide.

1. ESR

At 1 K the resonance lines in this magnetically concentrated salt were between 1 and 2 kOe wide, thus the center of the lines could be determined to ± 100 Oe. For a rotation about the c-axis only one broad line, exhibiting no anisotropy, was observed. Figures 18 and 19 show the rotation pattern data for resonant fields in the ac plane for $\nu=10$ and 25 GHz. θ is the angle between the applied field and the c-axis.

The resonant frequencies plotted as a function of field applied parallel to c are given in Figure 20. Negative frequencies correspond to transitions observed at fields greater than the field at which the energy levels cross (Figure 26).

2. Magnetic Susceptibility

Figure 21 shows the reciprocal magnetic susceptibility measured parallel to the c and a axes plotted for $T < 4.2$ K. No anisotropy was observed in χ for rotations about c between 1-4 K. The magnetic susceptibility measured parallel to c and a for $T < 1.4$ K is plotted in Figure 22.

Figure 18. ESR rotation patterns in the ac plane($\theta=0^\circ$ is the c-axis) for $\text{NiI}_2 \cdot 6\text{H}_2\text{O}$ at $\nu=10.01$ GHz and $T=1.1$ K. The solid lines are the theoretical predictions.

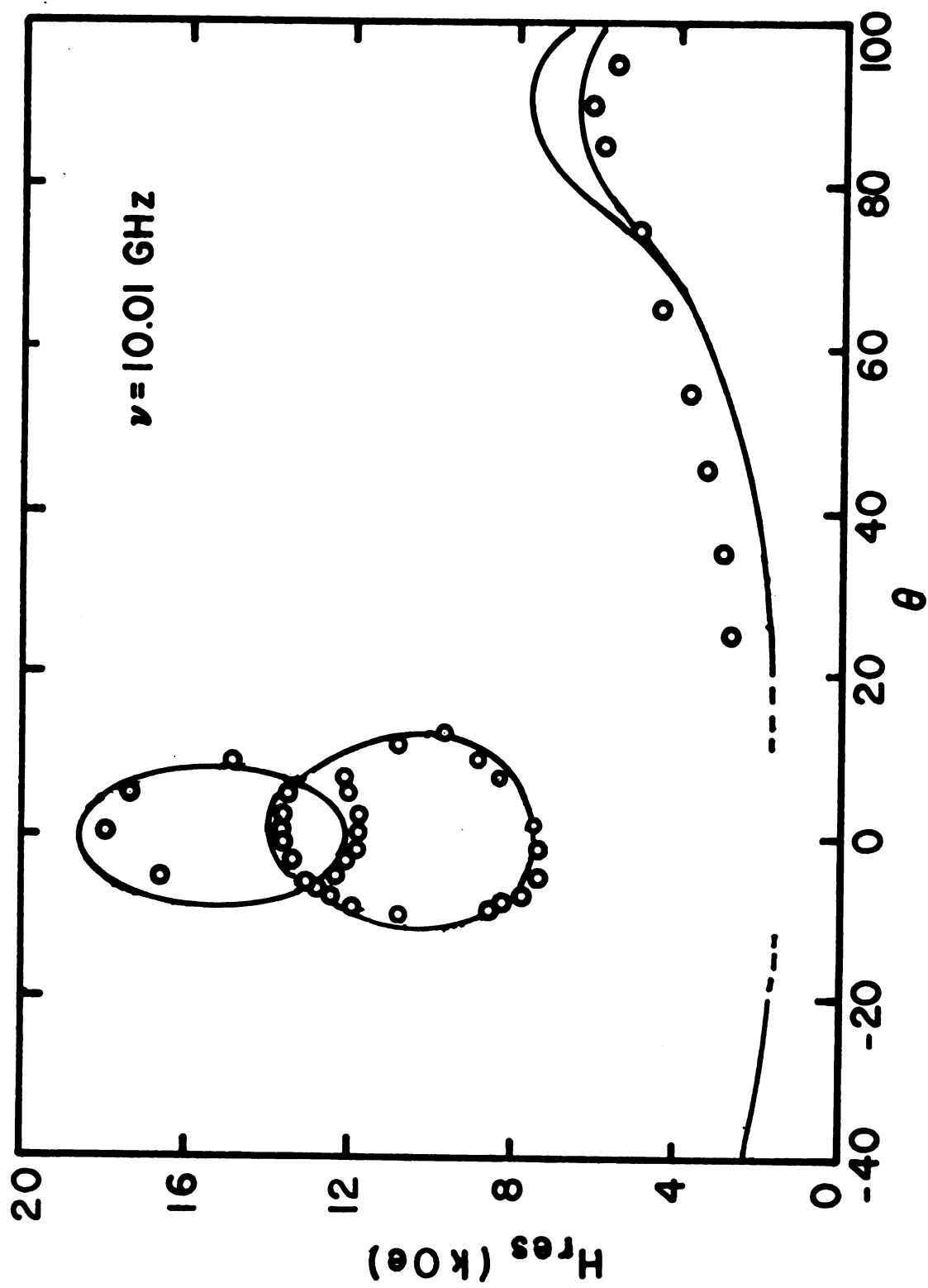


Figure 18

Figure 19. ESR rotation patterns in the ac plane ($\theta=0^\circ$ is the c-axis) for $\text{NiI}_2 \cdot 6\text{H}_2\text{O}$ at $\nu=24.45$ GHz and $T=1.1$ K. The solid lines are the theoretical predictions.

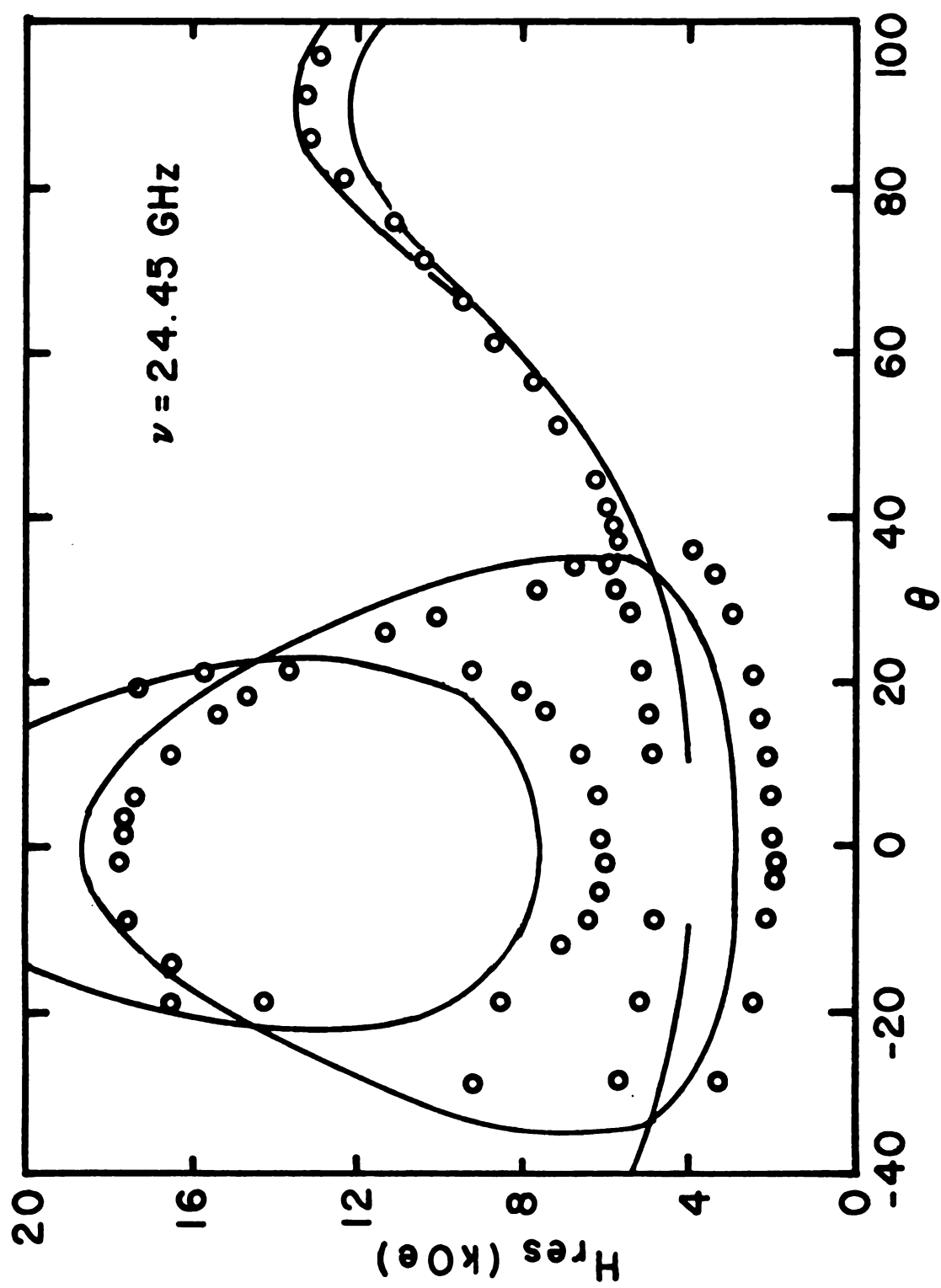


Figure 19

Figure 20. Resonant frequency vs. field applied parallel to the c-axis for $\text{NiI}_2 \cdot 6\text{H}_2\text{O}$. The solid and dashed lines are theoretical predictions.

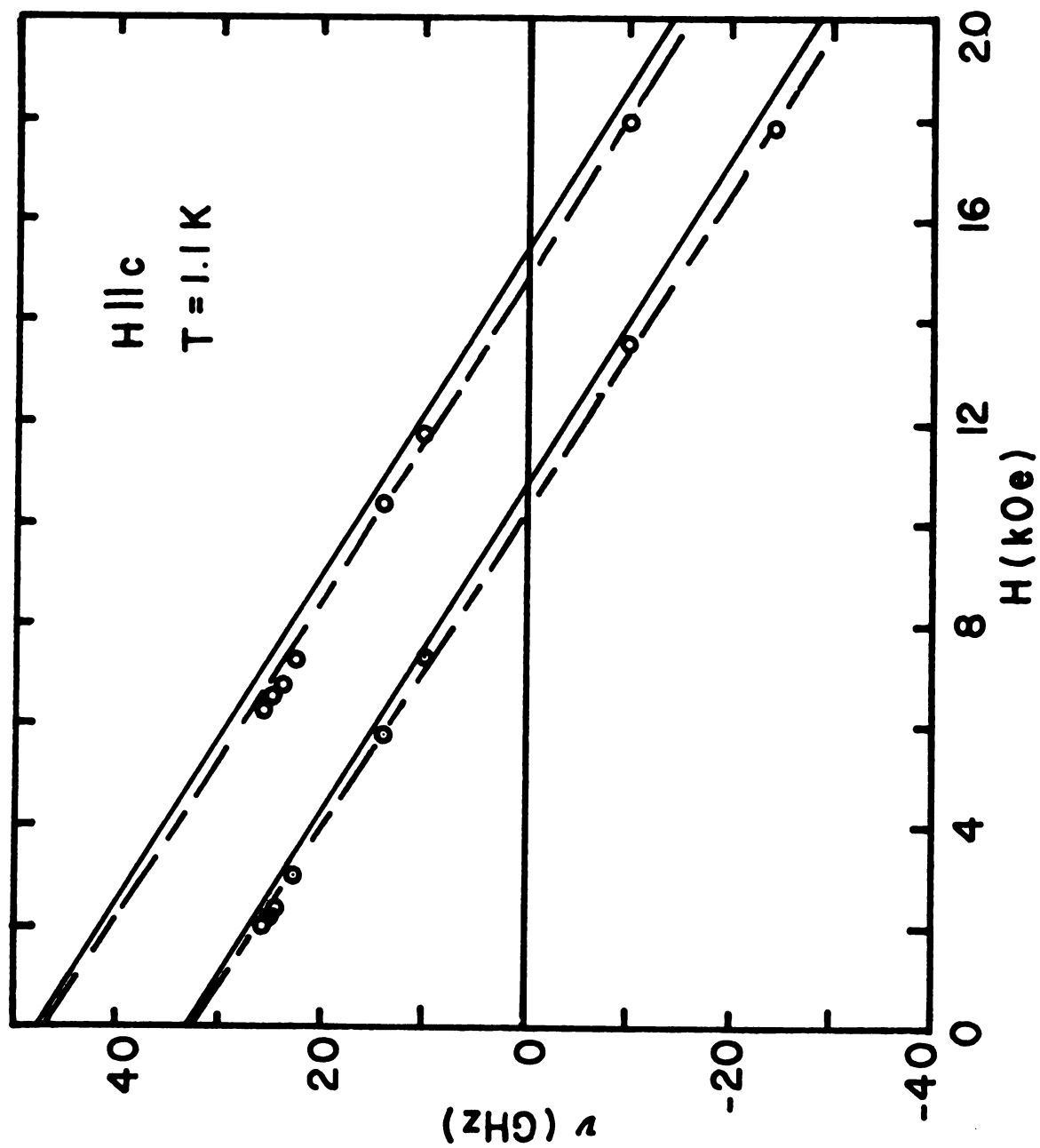


Figure 20

Figure 21. Inverse magnetic susceptibility of $\text{NiI}_2 \cdot 6\text{H}_2\text{O}$ measured parallel to the a and c axes. The solid lines are the theoretical results using equations (5.3)-(5.8).

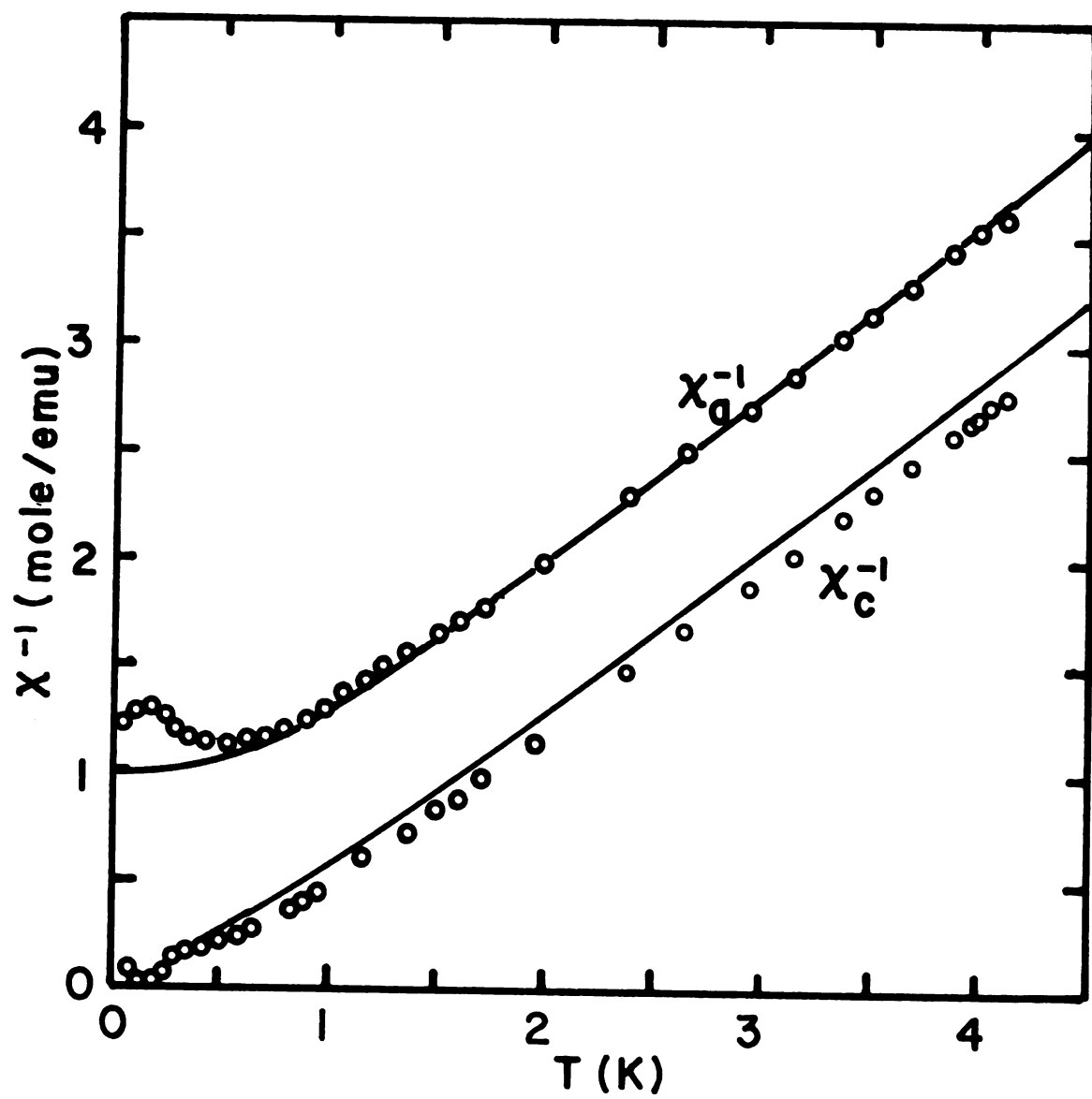


Figure 21

Figure 22. Magnetic susceptibility of $\text{NiI}_2 \cdot 6\text{H}_2\text{O}$ measured parallel to the a and c axes below 1.4 K.

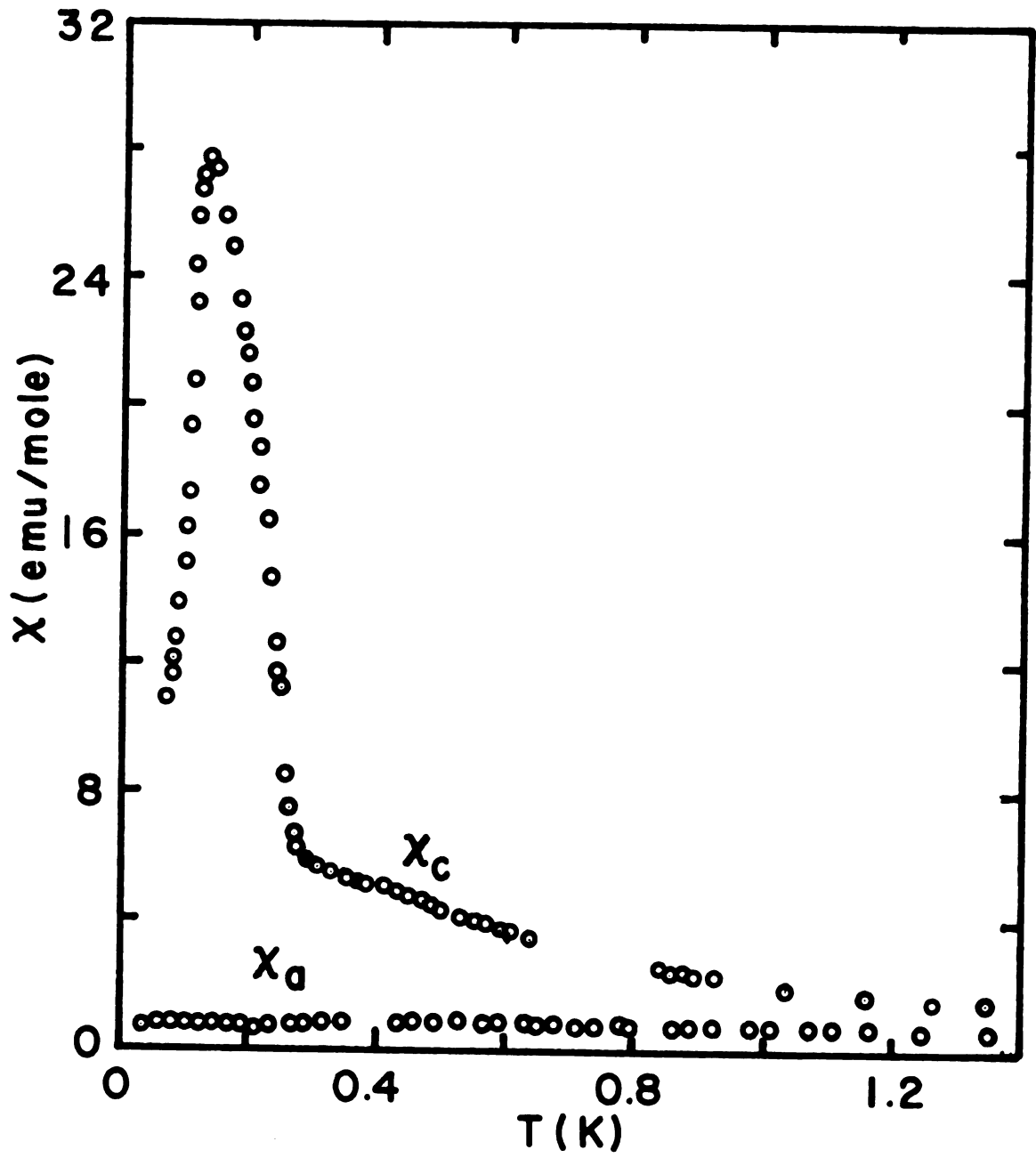


Figure 22

It is apparent that magnetic order occurs somewhere below 0.3 K. Defining the ordering temperature as the temperature with maximum positive $d\chi_c/dT$ gives $T_c = 0.120 \pm .005$ K. In considering χ_a the detailed behavior is best displayed in Figure 21 because the scale for Figure 22 necessary to display the peak in χ_c does not show the dip in χ_a at approximately 0.2 K.

3. NMR

Two pure quadrupole resonances were observed at $\nu_1 = 5.70 \pm .01$ MHz and $\nu_2 = 11.39 \pm .01$ MHz near 1 K. The line widths were approximately 250 kHz.

The results of NMR measurements near 1 K in applied field are summarized in Figures 23 and 24. In Figure 23 the data for resonant frequency versus field applied perpendicular to c is plotted. In this orientation the lines were sufficiently intense to permit a mapping of ν vs H over the entire range of experimental variables. Figure 24 shows ν vs H for $H \parallel c$. In this orientation the lines were much less intense and were not observed below 8 MHz.

Both the intensity and position of the NMR lines were strongly temperature dependent. Although the temperature dependence of the position is important in determining whether a transferred hyperfine term is present, the rapidly decreasing intensity of the lines allowed measurement of the temperature dependence only over a narrow temperature range. Figure 25 shows two data points and the theoretical calculation for the temperature dependence of the $m_I = +1/2 \longleftrightarrow m_I = -1/2$ resonance line.

Figure 23. ^{127}I NMR frequency vs. magnetic field applied perpendicular to c for $\text{NiI}_2 \cdot 6\text{H}_2\text{O}$.

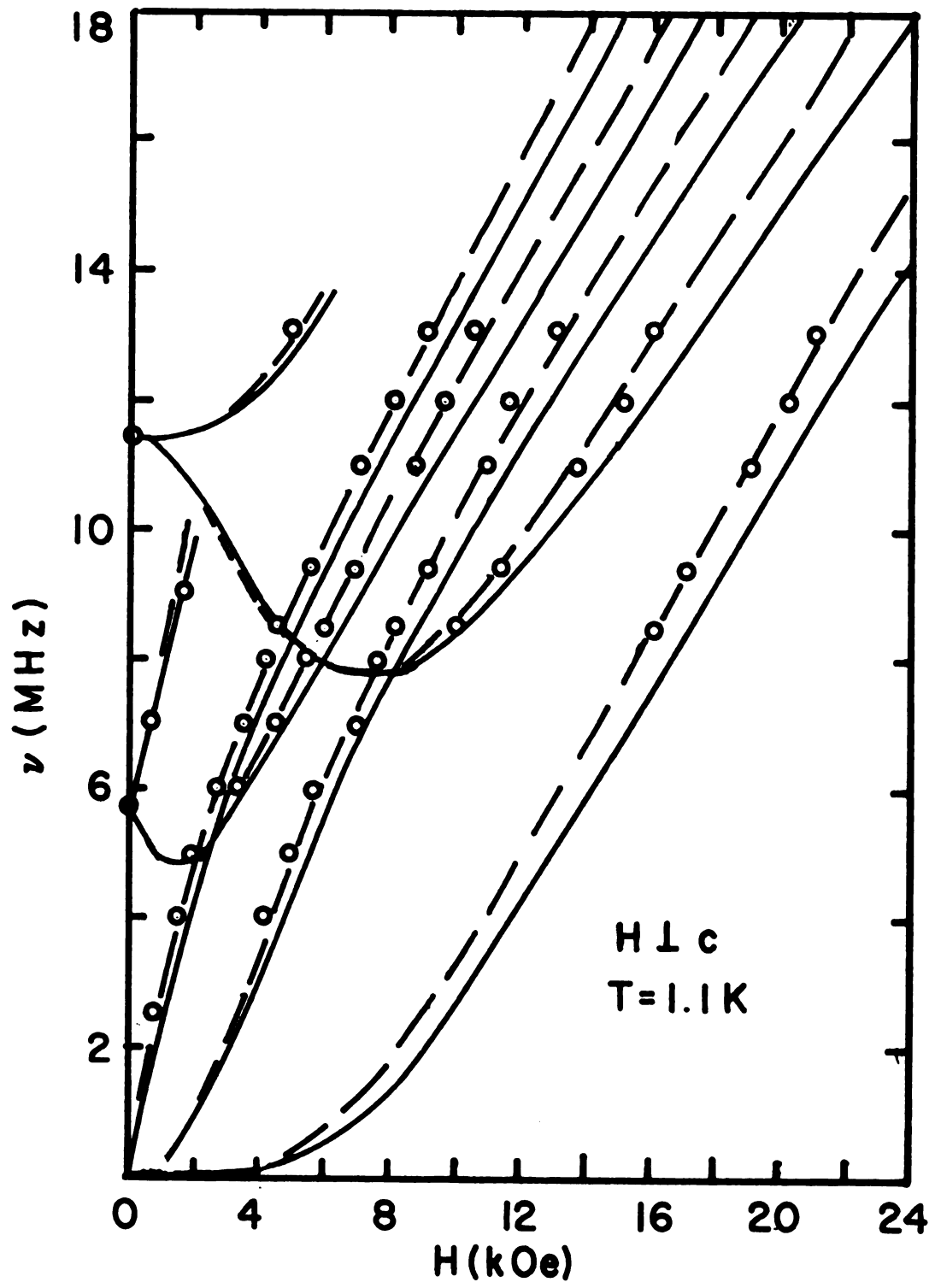


Figure 23

Figure 24. ^{127}I NMR frequency vs. magnetic field applied parallel to c for $\text{NiI}_2 \cdot 6\text{H}_2\text{O}$.

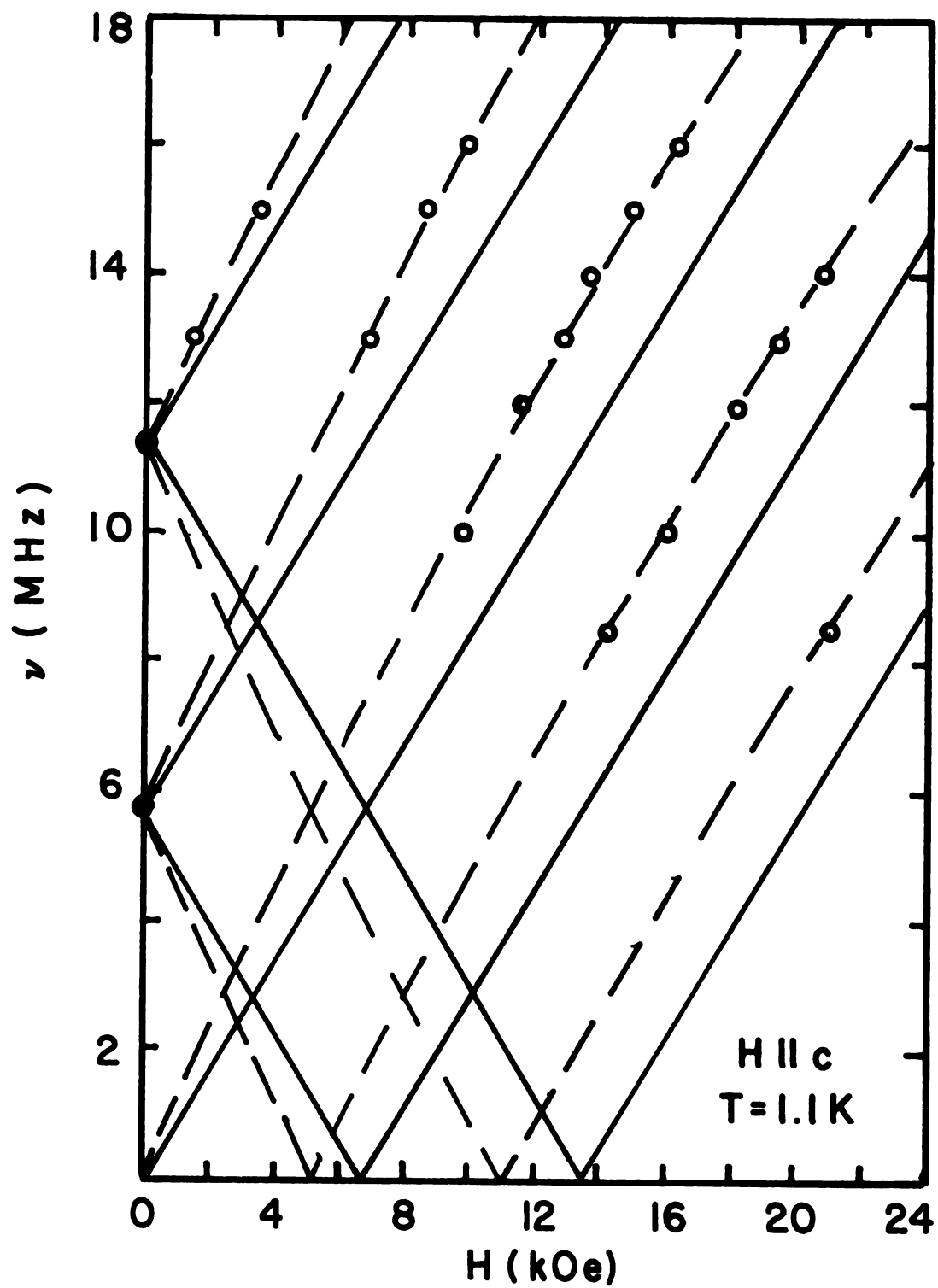


Figure 24

Figure 25. Temperature dependence of the $m_I=+1/2 \leftrightarrow m_I=-1/2$ resonance line of ^{127}I in $\text{NiI}_2 \cdot 6\text{H}_2\text{O}$ for $\nu=13.1$ MHz.

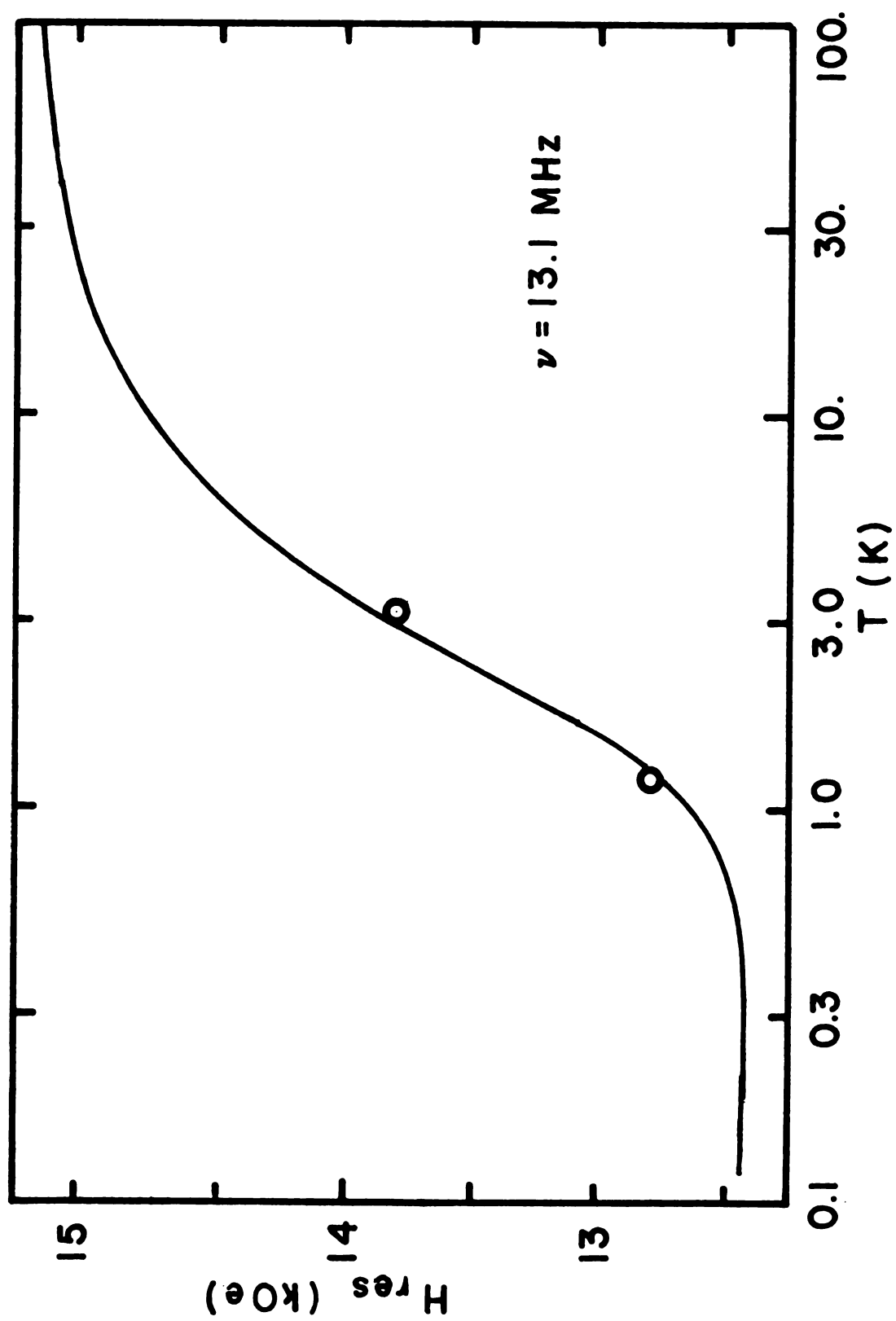


Figure 25

Although quantitative results were not obtained below $T_c = 0.12$ K, two zero-field NMR lines were observed. The frequency splitting varied with time(temperature) due to rf heating. The observed extremes of frequency were approximately 6.1 and 5.3 MHz.

C. Interpretation of Results

A number of authors²⁸⁻³¹ have successfully interpreted the magnetic properties of Ni^{++} salts in terms of a spin Hamiltonian(eq. 1.8) of the form

$$\mathcal{H}_S^i = -DS_{zi}^2 - E(S_{xi}^2 - S_{yi}^2) + g\mu_B \vec{H} \cdot \vec{S}_i \quad (5.1)$$

with $S=1$ and an isotropic $g \sim 2.25$. Schlapp and Penney³² have shown theoretically that a cubic crystal field, produced by octahedral coordination of the Ni^{++} ion lifts the orbital degeneracy leaving an orbital singlet lowest. A rhombic distortion of the field produces zero field splitting of the spin states described by the D and E terms in equation (5.1). The ESR transition frequencies, ν_i , are given by

$$\nu_i = \frac{|E_i - E_j|}{h} \quad (5.2)$$

where E_i and E_j are any two of the three eigenvalues of \mathcal{H}_S^i . The symmetry of the ESR rotation patterns indicates that the c axis corresponds to z. The absence of any anisotropy in the plane normal to c is conclusive evidence that the x and y axes are equivalent; indicating $E=0$. The ESR patterns also give conclusive evidence that there are two nonequivalent Ni sites each having z parallel to c and $E=0$ but with different

magnitudes for D. Figure 26 shows the energy levels for the Hamiltonian (5.1) with H applied along c. The ESR results do not reveal the sign of D but the figure is drawn assuming $D > 0$; implying the doublet lies lowest in zero field. Selection rules allow only $\Delta m_S = 1$ transitions for this orientation. The two "eggs" observed in the rotation patterns (Figures 18 and 19) and the two lines in the frequency vs field data (Figure 20) can only be explained by assuming two different Ni sites.

Using equations (5.1) and (5.2) the theoretical results shown in Figures 18 and 19 are obtained using $g_1 = g_2 = 2.22$, $E_1 = E_2 = 0$, $D_1/k = 1.6$ K and $D_2/k = 2.3$ K. The same parameters give ν vs H_c shown as the solid lines in Figure 20.

The magnetic susceptibility can be calculated from the Hamiltonian (5.1) using the density operator defined in Section I. Doing this one obtains:

$$\chi_i = 2N \alpha g^2 \mu_B^2 \delta_i \quad (5.3)$$

where $i = x, y, z$,

$$\delta_z = \frac{1}{kT} \frac{e^{D/kT}}{2e^{D/kT} + 1}, \quad (5.4)$$

and

$$\delta_x = \delta_y = \frac{1}{D} \frac{e^{D/kT} - 1}{2e^{D/kT} + 1}. \quad (5.5)$$

Assuming 50% of the sites are characterized by D_1 and 50% by D_2 , the total susceptibility is given by

$$\chi_i = \frac{\chi_i^{(1)} + \chi_i^{(2)}}{2} \quad (5.6)$$

Figure 26. Energy level diagram of $\text{Ni}^{++}(\text{S}=1)$ as a function of magnetic field, H , parallel to z with $D>0$ (doublet lowest).

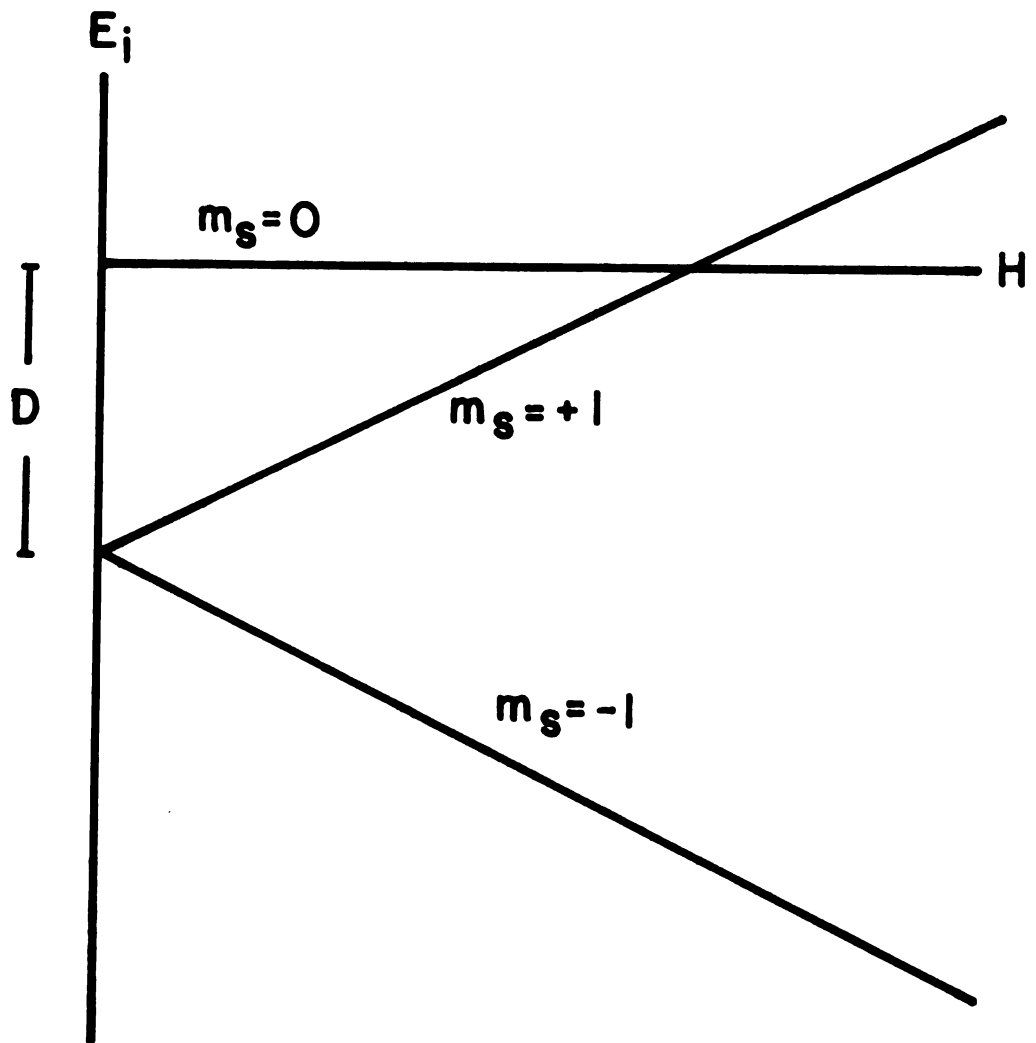


Figure 26

Equations (5.3) - (5.5) give $\chi_z > \chi_x = \chi_y$ if $D > 0$, and $\chi_z < \chi_x = \chi_y$ if $D < 0$. Equation (5.6) predicts that if D_1 and D_2 had opposite signs there would be very little difference between χ_c and χ_a . Figure 21 shows large anisotropy between χ_c and χ_a , with $\chi_c > \chi_a$; therefore, since the ESR showed z parallel to c , both D_1 and D_2 are assumed positive.

If the values of D_1 and D_2 found from the ESR are used in fitting χ , the agreement is quite good but the predicted magnitudes of χ_a and χ_c are somewhat low. Since the salt does order magnetically, a contribution due to exchange may be required. A simple way to include exchange in the molecular field approximation is to modify the Hamiltonian (5.1) as follows:

$$\mathcal{H}^i = -DS_{zi}^2 + g\mu_B \vec{H} \cdot \vec{S}_i - 2zJ \langle \vec{S} \rangle \cdot \vec{S}_i \quad (5.7)$$

Equation (5.3) becomes

$$\chi_i = \frac{2N_0 g^2 \mu_B^2 \delta_i}{1 - 2zJ\delta_i} \quad (5.8)$$

Using this expression in equation (5.6) with g , D_1 , D_2 given above and $2zJ/k = +0.05$ K gives the solid lines shown in Figure 21. The inclusion of a ferromagnetic exchange makes the agreement between experiment and theory for χ_a quite good but the theoretical results for χ_c are still less than the experimental data.

Including exchange in the description of χ suggests that it should be included in the interpretation of the ESR. McMillan and Opechowski³³ have calculated the shift in resonant

frequency away from the value determined by \mathcal{N}_S^i due to an exchange term, \mathcal{N}_{EX} , with $\mathcal{N}_{EX} \ll \mathcal{N}_S$ and $J/kT \ll 1$. The first term of the high temperature expansion for the change in frequency due to \mathcal{N}_{EX} is

$$h\langle\Delta\nu\rangle = 2zJ \frac{(e^{-E_1/kT} - e^{-E_2/kT})}{Z} \quad (5.9)$$

where, for $H \parallel c$, E_1 and E_2 are the eigenvalues of \mathcal{N}_S^i for $m_S = -1$ and $m_S = 0$ respectively and Z is the partition function calculated from \mathcal{N}_S^i . The results for ν vs H obtained with this correction with the values used to calculate χ are shown as dashed lines in Figure 20. The correction is not shown for the rotation patterns; however, the small shift to lower fields that it gives will improve the agreement between theory and experiment for most of the patterns.

Demagnetizing and dipole-dipole corrections also need to be considered; however, they are quite small and tend to cancel because they have opposite signs. Thus it appears the magnetic properties of $\text{NiI}_2 \cdot 6\text{H}_2\text{O}$ in its paramagnetic state are due to two nonequivalent Ni ion sites having crystal field splitting characterized by $D_1/k = 1.6$ K and $D_2/k = 2.3$ K. In addition, a weak ferromagnetic exchange between the spins is also present with $2zJ/k = +0.05$ K.

The behavior in the ordered state is more confusing. The large value of χ_c at approximately 0.2 K is indicative of magnetic moments parallel to c , which is consistent with the single ion anisotropy prediction for $D > 0$ (doublet lowest) and $z \parallel c$. The presence of ferromagnetic exchange (coupling the

moments) is also in agreement with the large value of χ_c . The susceptibility could not be measured to sufficiently low temperature to determine the nature of the ordered state. If χ_c continues to decrease so that $\chi_c = \chi_{||} \rightarrow 0$ as $T \rightarrow 0$ then the ordered state is probably antiferromagnetic due to a weak antiferromagnetic exchange as in the case of $((\text{CH}_3)_3\text{NH})\text{CuCl}_3 \cdot 2\text{H}_2\text{O}$. If χ_c does not continue to decrease the ordered state is probably consistent with the ferromagnetic exchange observed in the paramagnetic state being three dimensional. The fact that χ_a is increasing at the lowest temperatures obtained is inconsistent with simple antiferromagnetic order but is not conclusive.

The transition temperature predicted by the MF result,

$$T_c = \frac{2zJS(S+1)}{3k} , \quad (5.10)$$

with $2zJ/k = 0.05$ K is $T_c \sim 0.03$ K, considerably below the observed $T_c = 0.12$ K. Although molecular field estimates of transition temperatures are notoriously unreliable, the low value of T_c predicted may indicate that additional exchange, raising the value of T_c , is present.

The interpretation of the NMR measurements in the paramagnetic state does not expand greatly on the understanding of the magnetic properties of the system, but the ^{127}I resonances do include some points of intrinsic interest. A nuclear spin Hamiltonian to describe a nucleus of spin $I = 5/2$ like ^{127}I is analogous in many ways to the electron spin Hamiltonian which describes the Ni^{++} ion, equation (5.1).

The Hamiltonian can be written

$$\mathcal{H}_N = \mathcal{H}_Q + \mathcal{H}_D, \quad (5.11)$$

where \mathcal{H}_Q is the nuclear electric quadrupole term and \mathcal{H}_D is the nuclear magnetic dipole term.

\mathcal{H}_Q involves the interaction of the nuclear quadrupole moment with the electric field gradient at the nucleus.

Dropping constant terms, \mathcal{H}_Q can be written,

$$\mathcal{H}_Q = \frac{h\nu_Q}{2} I_z^2 + \frac{h\nu_Q}{6} (I_x^2 - I_y^2) \quad (5.12)$$

where $\nu_Q \equiv 3e^2qQ/2I(2I-1)h$. Q is the scalar nuclear quadrupole moment, eq is the axial component of the electric field gradient, and η is a measure of the nonaxial nature of the field gradient. The similarity between these two terms and the D and E terms in equation (5.1) is quite apparent.

The dipole term, \mathcal{H}_D , includes the interaction of the nuclear magnetic dipole moment with the external magnetic field and all internally produced magnetic fields. Therefore

$$\mathcal{H}_D = -\gamma_N \hbar \vec{I} \cdot \vec{H}_i \quad (5.13)$$

where γ_N is the nuclear gyromagnetic ratio. It is assumed that the contributions to \vec{H}_i can be separated into those due to external fields, those due to electrons in I^- orbitals, and those due to electrons external to the I^- . Thus,

$$\vec{H}_i = \vec{H}_0 - (\gamma_N \hbar)^{-1} \vec{A} \cdot \vec{S} + 2\mu_B \langle r^{-3} \rangle \vec{L} + \vec{H}_d \quad (5.14)$$

\vec{H}_0 is the applied field. In this case the magnetic hyperfine coupling tensor, \vec{A} , represents the transferred hyperfine

contribution due to the unpaired spin present in I^- orbitals because they overlap the Ni^{++} 3d wavefunctions. The orbital hyperfine term is assumed to be small. The term \vec{H}_d includes fields due to all the other electronic magnetic dipoles in the crystal including shape dependent demagnetizing fields. In this case it is quite small and can be neglected as it was for \mathcal{H}_S . Since the correlation times for the electrons are usually much shorter than the nuclear precession time, the nuclear magnetization responds to the average electronic field so $\vec{S} \rightarrow \langle \vec{S} \rangle$. Neglecting the last two terms equation (5.14) becomes

$$\vec{H}_i = \vec{H}_0 + (\gamma_N \hbar)^{-1} \vec{A} \cdot \langle \vec{S} \rangle \quad (5.15)$$

Often the nuclear spin Hamiltonian is solved for either the low field ($\mathcal{H}_D < \mathcal{H}_Q$) or the high field ($\mathcal{H}_D > \mathcal{H}_Q$) case using a perturbation calculation^{34,36}. Since the NMR data presented here was taken over a range of fields covering both cases it is necessary to solve for the eigenvalues of \mathcal{H}_N exactly³⁷.

Since $\vec{H}_i = 0$ in the paramagnetic state when $\vec{H}_0 = 0$, the two $\Delta m_S = 1$ resonances observed in zero field uniquely determine ν_Q and η as $\nu_Q = 5.70$ MHz and $\eta = 0$. With $\eta = 0$ equation (5.12) is axially symmetric and no anisotropy is expected or observed in the xy plane. This is an unusually low value of ν_Q for ^{127}I . With $Q = -0.75 \times 10^{-24} \text{ cm}^2$ it is customary to find the pure quadrupole resonances at frequencies greater than 100 MHz. This implies that the electric field gradient at the I site is small with correspondingly high symmetry. It should be

noted that only one set of I resonances was observed. The two I sites predicted by the room temperature X-ray structure have the same symmetry and thus should have the same value for ν_Q and η . However the apparent doubling of the unit cell indicated by ESR might produce two pairs of I sites. Since only one set of lines were observed, either the I sites still all have the same electric field gradient, or the other site has a more typical value of ν_Q for ^{127}I and is beyond the experimental range of frequencies available.

Assuming $\vec{A}=0$ as a first approximation, then $\vec{H}_i = \vec{H}_0$ and the resonant frequencies can be determined as a function of field from the eigenvalues of \mathcal{H}_N . The solutions, for $H_0 \perp c$, are shown as the solid lines in Figure 23. The results for $H_0 \parallel c$ are shown in Figure 24. At high fields the Zeeman line is split by the quadrupole interaction into five lines with the splitting for H parallel to c much larger than that for H perpendicular to c. Although the theory is qualitatively correct, the data appears at lower fields than predicted. The agreement between theory and experiment can be improved by including the hyperfine term in equation (5.15). Assume \vec{A} to be axially symmetric with diagonal elements denoted $A_{xx}=A_{yy}=A_{\perp}$ and $A_{zz}=A_{\parallel}$. Then for $H \parallel c$, $\langle \vec{S} \rangle = \langle S_z \rangle$ and

$$H_{ic} = H_{oc} + (\gamma_N \hbar)^{-1} A_{\parallel} \langle S_z \rangle. \quad (5.16)$$

Similarly,

$$H_{ia} = H_{oa} + (\gamma_N \hbar)^{-1} 2A_{\perp} \langle S_x \rangle. \quad (5.17)$$

To determine \vec{A} in the paramagnetic state it is normally

sufficient³⁸ to obtain the components of $\langle \vec{S} \rangle$ from

$$\langle S_i \rangle = \frac{M_i}{N_O g \mu_B} \sim \frac{\chi_i H}{N_O g \mu_B}, \quad (5.18)$$

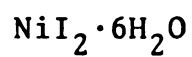
where $i = x$ and z . However in this case, the applied field produces saturation effects so that $\langle S_i \rangle$ cannot be determined in this way. The theoretical expressions for $\langle S_i \rangle$ found using the density operator and Hamiltonian (5.1) are used instead. The results obtained using $A = 2.30$ MHz and $A = 0.55$ MHz at $T = 1.1$ K are shown in Figures 23 and 24 as dashed lines. A summary of the quadrupole and hyperfine constants are given in Table II.

The contribution due to the hyperfine term should have the same temperature dependence as $\langle \vec{S} \rangle$. In Figure 25 the predicted temperature dependence of the resonant field is shown for the $m_z = 1/2 \longleftrightarrow m_z = -1/2$ transition with $H \parallel c$ at fixed frequency. The approximate value of A_{\parallel} was determined from the lower temperature point, but the agreement with the other point and that found for the other lines using the same value of A_{\parallel} is very reasonable.

It is interesting and confusing to note that the agreement between theory and experiment for the intensities of the NMR transitions is very good for $H \perp c$ and very poor for $H \parallel c$. The theoretical intensities are determined by the square of the transition operator matrix elements between eigenfunctions of \mathcal{H}_N (neglecting \vec{A}). Theory predicts the two cases should have approximately the same intensity whereas the experimental lines for $H \parallel c$ are much weaker. No explanation of this

Table II

^{127}I Quadrupole and Hyperfine Constants for Paramagnetic



$$\nu_Q = 5.70 \pm 0.01 \text{ MHz}$$

$$\eta = 0.00 \pm 0.03$$

$$A_{\parallel} = 2.30 \pm 0.01 \text{ MHz}$$

$$A_{\perp} = 0.55 \pm 0.10 \text{ MHz}$$

behavior has been found.

Most of the NMR results do not apply directly to the description of the magnetic properties of nickel iodide, but the presence of the transferred hyperfine term is consistent with the existence of exchange. The exchange is most likely superexchange through the I^- , requiring that the Ni^{++} unpaired electron wavefunctions overlap the I^- wavefunctions.

Attempts to extend these quantitative measurements into the ordered state were unsuccessful. The only two lines observed were split about ν_Q as expected in a weak internal magnetic field (See Figures 23 and 24), but the temperature dependence could not be measured.

In conclusion the magnetic properties of $NiI_2 \cdot 6H_2O$ are explained by two inequivalent Ni^{++} ion sites described by $D_1/k=1.6$ K, $D_2/k=2.3$ K, $g=2.22$, and a weak ferromagnetic exchange with $2zJ/k=+0.05$ K. The exchange is most likely superexchange through the I^- . Below $T_c=0.12$ K the salt is apparently in a three dimensional ordered state with the spins most likely parallel to c. The nature of the ordered state could not be determined.

VI. CONCLUSIONS

Experimental investigations of three transition metal salts have been discussed. The measurements included ESR, NMR and magnetic susceptibility.

The paramagnetic behavior of all three salts can be understood in terms of existing theoretical models.

The two trimethylamine salts exhibit low-dimensionality. While the cobalt salt is nearly one dimensional with the ferromagnetic exchange along the chains more than ten times what it is between the chains¹, the copper salt is a two-dimensional square ferromagnetic system. The exchange in the cobalt salt is Ising exchange while in the copper it is isotropic Heisenberg exchange.

The paramagnetic behavior of nickel iodide is dominated by the zero field splitting of the single ion spin states. The effective dimensionality of the exchange cannot be determined because the effects due to exchange are masked by the single ion effects.

The models for the ordered state give qualitative results for the trimethylamine salts, while the data is insufficient to determine the nature of the ordered state of nickel iodide.

$((\text{CH}_3)_3\text{NH})\text{CuCl}_3 \cdot 2\text{H}_2\text{O}$ has ferromagnetic sheets coupled antiferromagnetically. The ordered state has no net moment but the successive spins in the chains are canted slightly away from the *a* axis.

$((\text{CH}_3)_3\text{NH})\text{CoCl}_3 \cdot 2\text{H}_2\text{O}$ in zero field is also a canted antiferromagnet. However, it displays unusual metamagnetic

behavior in applied field. The phenomenological model proposed by Spence² provides a qualitative understanding of this behavior, but does not contain any temperature dependence.

The experimental data in the ordered state of $\text{NiI}_2 \cdot 6\text{H}_2\text{O}$ is rather limited and indicates only that the system is ordered and has the spins parallel to the single ion preferred direction. Whether the state is ferromagnetic or antiferromagnetic is unclear.

Several recommendations for additional work on these salts can be made.

The high temperature expansion for the susceptibility of a rectangular Heisenberg lattice might give a better fit to χ for the copper salt. In addition, a molecular field treatment of the layered antiferromagnet with canting might give more quantitative results for the ordered state.

A model for the metamagnetic behavior of trimethylamine cobalt chloride which includes temperature and possibly domains, would be very interesting. If such a model were obtained, additional experimental work would also be indicated.

Further work on nickel iodide might be worthwhile, but of greater interest would be a nickel salt in which the exchange energy were larger so that the effects due to both exchange and zero field splitting would be present in a more reasonable temperature range. The presence of low-dimensionality in such a case would be of even greater interest.

REFERENCES

REFERENCES

1. D. B. Losee, J. N. McElearney, G. E. Shankle, R. N. Carlin, P. J. Cresswell, and W. T. Robinson, *Phys. Rev.* B8, 2185 (1973).
2. R. D. Spence and A. C. Botterman, *Phys. Rev.* B9, 2993 (1974).
3. R. M. White, Quantum Theory of Magnetism, (McGraw-Hill, New York, 1970).
4. D. H. Martin, Magnetism in Solids, (Iliffe Books, London, 1967).
5. J. S. Smart, Effective Field Theories of Magnetism, (W. B. Saunders, Philadelphia, 1966).
6. G. S. Rushbrooke and P. J. Wood, *Mol. Phys.* 1, 257 (1958).
7. W. R. Abel, A. C. Anderson, and J. C. Wheatley, *Rev. Sci. Inst.* 35, 444 (1964).
8. C. W. Fairall, "The Anisotropic Antiferromagnet-Theory and Experiment," Thesis, Michigan State University (1970).
9. Cryotronics, Inc., High Bridge, New Jersey.
10. C. W. Fairall, D. D. Swinehart, and J. A. Cowen, *J. Appl. Phys.* 41, 2509 (1970).
11. S. I. Parks, "NMR in Paramagnetic NdBr_3 and UI_3 and in Antiferromagnetic UI_3 ," Thesis, Florida State University (1967).
12. Princeton Applied Research Corporation, Princeton, New Jersey.
13. D. B. Losee, J. N. McElearney, A. Siegel, R. L. Carlin, A. A. Khan, J. P. Roux, and W. J. James, *Phys. Rev.* B6, 4342 (1972).
14. P. Groth, Chemische Kristallographie (Wilhelm Englemann, Leipzig).
15. D. S. Schonland, *Proc. Phys. Soc. Lond.* 73, 788 (1959).
16. R. E. Dietz, F. R. Merritt, R. Dingle, D. Hone, B. G. Silbernagel, and P. M. Richards, *Phys. Rev. Lett.* 26, 1186 (1971).
17. G. A. Baker, Jr., H. E. Gilbert, J. Eve, and G. S. Rushbrooke, *Phys. Lett.* A25, 207 (1967).

18. J. C. Bonner and M. E. Fisher, Phys. Rev. 135, A640 (1964).
19. L. Néel, Nuovo Cimento Suppl. 6, 942 (1957).
20. J. Kanamori, Prog. Theor. Phys. 20, 890 (1958).
21. B. R. Heap, Proc. Phys. Soc. Lond. 80, 248 (1962).
22. L. Berger and S. A. Friedberg, Phys. Rev. 136, A158 (1964).
23. L. J. DeJongh, W. D. van Amstel, and A. R. Miedema, Physica (Utr.) 58, 277 (1972).
24. I. F. Silvera, J. H. M. Thornley, and M. Tinkham, Phys. Rev. 136, A695 (1964).
25. W. Opechowski and R. Guccione, in Magnetism, edited by G. T. Rado and H. Suhl (Academic Press, New York, 1965), Vol. 2A, Chapter 3.
26. J. A. Osborn, Phys. Rev. 67, 351 (1945).
27. M. Gaudin-Louër and D. Weigel, C. R. Acad. Sc. Paris, 264 B895 (1967).
28. J. H. E. Griffiths and J. Owen, Proc. Roy. Soc. A213, 459 (1952).
29. K. W. H. Stevens, Proc. Roy. Soc. A214, 237 (1952).
30. T. Haseda and M. Date, J. Phys. Soc. Japan 13, 175 (1958).
31. T. Watanabe, J. Phys. Soc. Japan 17, 1856 (1962).
32. R. Schlapp and W. G. Penney, Phys. Rev. 42, 666 (1932).
33. M. McMillan and W. Opechowski, Can. J. Phys. 38, 1168 (1960).
34. T. P. Das and E. L. Hahn, Nuclear Quadrupole Resonance Spectroscopy, Solid State Physics, Suppl. 1 (Academic Press, New York, 1958).
35. A. Narath, Phys. Rev. 140, A552 (1965).
36. M. H. Cohen and F. Reif, "Nuclear Quadrupole Effects in Nuclear Magnetic Resonance," Solid State Physics, 5, 321 (1957).
37. G. Lamarche and G. M. Volkoff, Can J. Phys. 31, 1010(1953).
38. R. D. Spence, J. A. Casey, and V. Nagarajan, Phys. Rev. 181, 488 (1969).

MICHIGAN STATE UNIVERSITY LIBRARIES



3 1293 03145 9971